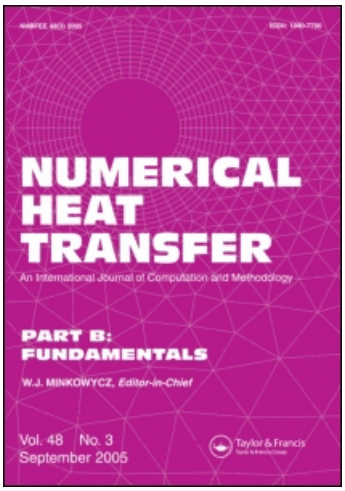

Numerical Heat Transfer, Part B: Fundamentals
Publication details, including instructions for authors and subscription information:
http://www.informaworld.com/smpp/title~content=t713723316

NONLINEAR SUBGRID EMBEDDED FINITE-ELEMENT BASIS FOR STEADY MONOTONE CFD SOLUTIONS, PART II: BENCHMARK NAVIER-STOKES SOLUTIONS

Subrata Roy [a]; A. J. Baker [b]
[a] Computational Mechanics, Knoxuille, Tennessee, USA [b] Mechanical and Aerospace Engineering and Engineering Science, University of Tennessee, Knoxuille, Tennessee, USA

Online Publication Date: 01 January 1998

To cite this Article Roy, Subrata and Baker, A. J.(1998)'NONLINEAR SUBGRID EMBEDDED FINITE-ELEMENT BASIS FOR STEADY MONOTONE CFD SOLUTIONS, PART II: BENCHMARK NAVIER-STOKES SOLUTIONS',Numerical Heat Transfer, Part B: Fundamentals,33:1,5 — 36
To link to this Article: DOI: 10.1080/10407799808915021
URL: http://dx.doi.org/10.1080/10407799808915021

NONLINEAR SUBGRID EMBEDDED FINITE-ELEMENT BASIS FOR STEADY MONOTONE CFD SOLUTIONS, PART II: BENCHMARK NAVIER-STOKES SOLUTIONS

Subrata Roy
Computational Mechanics Corporation, Knoxville, Tennessee, USA

A. J. Baker
Mechanical and Aerospace Engineering and Engineering Science, University of Tennessee, Knoxville, Tennessee, USA

A nonlinear subgrid embedded (SGM) finite-element basis is established for generating monotone solutions via a CFD weak statement algorithm. The theory confirms that only the Navier-Stokes dissipative flux vector term is appropriate for implementation of the SGM, which thereafter employs element-level static condensation for efficiency and nodal-rank homogeniety. Numerical results for select benchmark compressible and incompressible steady-state Navier-Stokes problem definitions are presented, confirming theoretical prediction for attainment of monotone solutions devoid of excess numerical diffusion on minimal-degree-of-freedom meshes.

INTRODUCTION

Consider the Navier-Stokes conservation law system for state variable $q = q(x_j, t)$ of the form

$$\mathscr{L}(q) = \frac{\partial q}{\partial t} + \frac{\partial}{\partial x_j}(\mathbf{f}_j - \mathbf{f}_j^v) - s = 0 \qquad \text{on } \Omega \times t \subset \mathscr{R}^d \times \mathscr{R}^+, 1 \leqslant j \leqslant d \quad (1a)$$

$$\mathscr{L}_a(q_a) = -\frac{\partial^2 q_a}{\partial x_j^2} - s(q) = 0 \quad (1b)$$

where $q = \{\rho, m_i, E\}$ or $\{u_i, \Theta\}$ for compressible or incompressible fluids, while $\mathbf{f}_j = f(u_j, q, p)$ and $\mathbf{f}_j^v = f[\epsilon(\partial q/\partial x_j)]$ are the kinetic and dissipative flux vectors, respectively. For compressible flow, pressure $p = p(q)$ is characterized by a thermodynamic gas law, the convection velocity definition is $u_i = m_i/\rho$, and $\epsilon > 0$ is typically inverse Reynolds number while s is the source. For incompressible flows,

Received 27 January 1997; accepted 1 August 1997.

Subrata Roy is currently at CASE Corporation, 7S. 600 County Line Road, Burr Ridge, IL 60521-6975, USA. E-mail: rsubrata@casecorp.com

Address correspondence to Professor A. J. Baker, Engineering Science and Mechanics, 310 Perkins Hall, Knoxville, TN 37996-2030, USA.

Numerical Heat Transfer, Part B, 33:5–36, 1998

1040–7790/98 $12.00 + .00

NOMENCLATURE

A	scalar constant	Q	discrete state variable
$c, \mathbf{c}_j$	continuum SGM parameter (set)	$r, \mathbf{r}_j, r_{ij}$	distributed SGM parameter (set)
d	dimension of the problem	R	statically reduced matrix
$\det_e$	transformation matrix-determinant	$\{R\}$	solution residual vector
$[D_k]_e$	Lagrange diffusion matrix	$\Re^d$	real d-dimensional space
$[D_S]_e$	SGM diffusion matrix	$\Re^+$	temporal half-space
e	finite element	Re	Reynolds number
E	volume-specific total energy	s	source term
$f(\cdot)$	function of $(\cdot)$	S	SGM polynomial degree
$\mathbf{f}_j$	kinematic flux vector	S_e	element matrix assembly operator
$\mathbf{f}_j^v$	viscous flux vector	t	time
$\mathscr{F}, \mathscr{F}_{ij}$	SGM (correlation) function	T	temperature
$\{FQ\}$	Newton residual vector	u_j, U	velocity vector
g, g_i	SGM element embedding function	$[U]_e$	convection matrix
$\{G\}$	nodally distributed SGM vector	$\|U\|$	absolute value of velocity U
h, h_e, h_{ij}	finite-element length measure	V_e	volume (area) of a finite element
[JAC]	Jacobian matrix	x_j	spatial coordinates
k	Lagrange Polynomial degree	α	SGM polynomial function of c
L, R	element left/right of node j	β	artificial diffusion coefficient
$\mathscr{L}, \mathscr{L}_a$	partial differential equation operator	δ_{ij}	Kronecker delta
		Δt	computational time step
m	momentum flux	ϵ, ϵ_i	physical diffusion coefficient
$[M]$	assembled mass (interpolation) matrix	ζ	local normalized coordinate
		η, η_i	local natural coordinate
$\{N_k\}$	Lagrange basis function of degree k	θ	implicitness parameter
$\{N_S\}$	SGM basis function of degree S	ρ	density
p, P	static pressure	ϕ	continuity constraint
Pr	Prandtl number	ψ	streamfunction
q	continuum state variable	ω	vorticity
$\|q\|_E$	energy seminorm of q	Ω	domain

in (1b) the Laplacian operates on the auxilliary state variable $q_a = \{\phi, P\}^T$, where ϕ is a continuity constraint variable and P is kinematic pressure. Appropriate initial and boundary conditions close system (1) for the well-posed statement.

Computational difficulties occur as $\epsilon \to 0$, leading to occurence of "wall layer" solutions containing large local gradients. In computational fluid dynamics, (CFD), this is the natural occurrence for Reynolds number becoming large. Thus, even though the analytical solution to (1) remains smooth, monotone, and bounded, the spatially discretized CFD solution process becomes dominated by an oscillatory error mode, prompting the creation of artificial (numerical) diffusion mechanisms to control instability promoted by the inherent Navier-Stokes nonlinearity in $\mathbf{f}_j$.

The CFD algorithm research goal is to obtain an efficient, multidimensional, "arbitrary" grid algorithm that extracts an accurate, stable, and monotone solution for (1a) on a *practical mesh* for arbitrary ϵ. Stabilizing techniques such as artificial viscosity methods [1–3], flux correction operators [4–6], nonlinear interpolation *limiters* [7] for essentially nonoscillating (ENO) solution are available, but solutions

still exhibit oscillations near strictly local extrema and the multidimensional implementational can be problematical.

Solution-adaptive "p and h-p" forms of finite-element (FE) algorithms for handling solution mesh adaptation in an *automatic* manner have been extensively examined [8–14]. At a significant cost in increased algorithm operation count and storage requirements, several advantages including "unstructured meshing" accrue to these algorithms. However, solution monotonicity is typically not a theoretical ingredient in formulation of these algorithms.

In distinction, the subgrid embedded (SGM) finite-element basis theoretical development [15] addresses the fundamental issue of multidimensional *practical (coarse) grid solution accuracy with guaranteed monotonicity* and minimal (optimal) numerical diffusion. It is based on a genuinely nonlinear, nonhierarchical, high-degree finite-element basis for use in a discretized approximation of a weak statement algorithm. Verification for both linear and nonlinear convection-diffusion equation SGM finite-element solutions is documented in [15]; c.f. Figure 1, where small ϵ ($\mathscr{O}10^{-5}$) monotone and nodally accurate solutions are obtained on coarse grids.

The SGM basis construction is distinct from reported developments in the area of subgrid scale resolution, including hierarchical (h-p) elements [16] and nodeless bubble functions [17]. The SGM development employs strictly classical Lagrange basis methodology, and the SGM basis is applicable *only* to the dissipative flux vector term $\mathbf{f}_j^v$ in (1a) [18]. The discretized kinematic flux vector $\mathbf{f}_j$ remains a "centered" construction via the parent strictly Galerkin weak statement.

The key efficiency ingredient of the SGM element is reduction to linear basis element matrix rank for any embedded degree. This is in sharp contrast to conventional enriched basis finite-element/finite-difference algorithms, as the SGM element strictly contains matrix order escalation, hence increased computer resource demands. The results reported here are companion to [15], and document algorithm performance for steady-state solutions of the Navier-Stokes equations (1a)–(1b) for quasi-1D compressible and 2D incompressible benchmark problem statements.

NAVIER-STOKES CONSERVATION LAW FORMS

Three distinct formulations for the NS system (1a)–(1b) are considered in this article. The compressible flow benchmark is an off-design de Laval nozzle flow in a quasi-1D viscous specification. Hence,

$$q = \begin{Bmatrix} \rho \\ m \\ E \end{Bmatrix} \qquad f_j = f_1 = \begin{Bmatrix} m \\ \dfrac{m^2}{\rho} + p \\ \dfrac{(E+p)m}{\rho} \end{Bmatrix} \qquad f_j^v = f_1^v = \begin{Bmatrix} 0 \\ \dfrac{4}{3\,\mathrm{Re}} \dfrac{\partial u}{\partial x} \\ \dfrac{7}{2\,\mathrm{Pe}} \dfrac{\partial T}{\partial x} + \dfrac{2}{\mathrm{Re}} u \dfrac{\partial u}{\partial x} \end{Bmatrix} \tag{2a}$$

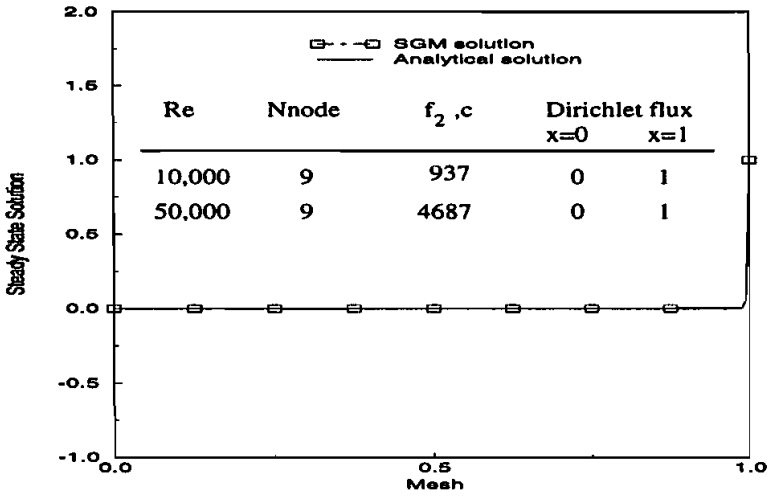

(*a*)

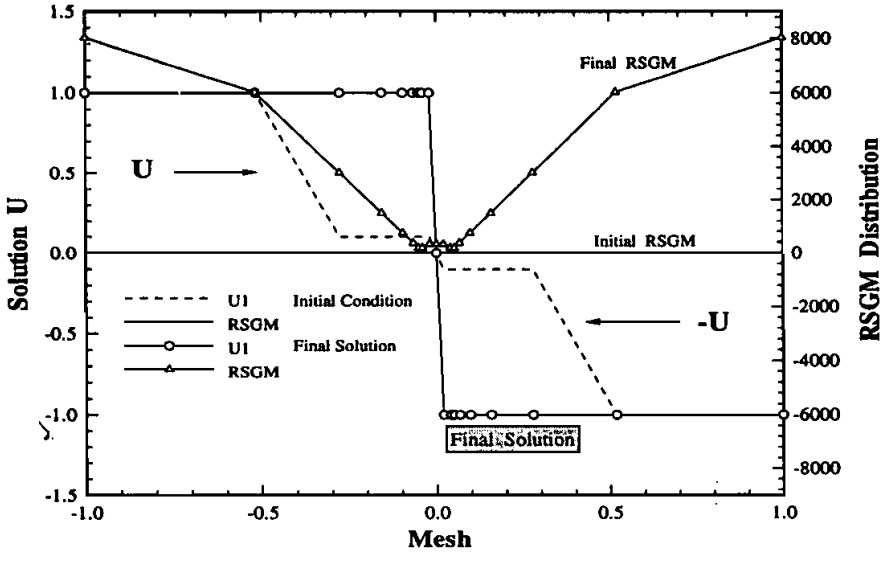

(*b*)

Figure 1. SGM element steady-state solutions for convection-diffusion verification problems [15]. (*a*) Linear Peclet problem, $1/\epsilon = \text{Pe} \leqslant 5 \times 10^4$; (*b*) nonlinear Burgers initial and final solution at $1/\epsilon = \text{Re} = 10^5$.

$$s = \begin{Bmatrix} -m \dfrac{d \ln A(x)}{dx} \\ -\dfrac{m^2}{\rho} \dfrac{d \ln A(x)}{dx} \\ -\dfrac{(E+p)m}{\rho} \dfrac{d \ln A(x)}{dx} \end{Bmatrix} \tag{2b}$$

where ρ is density, m is momentum, pressure is $p = (\gamma - 1)(E - m^2/2\rho)$, E is volume-specific total energy, γ is the ratio of specific heats, and $A(x)$ is the nozzle cross-sectional area distribution.

The nondimensional groups in (2*a*)–(2*b*) and thereafter are the Reynolds and Prandtl numbers with definitions

$$\mathrm{Re} = \frac{L_{\mathrm{ref}} U_{\mathrm{ref}}}{\nu_{\mathrm{ref}}} \qquad \text{and} \qquad \mathrm{Pr} = \frac{\nu_{\mathrm{ref}} \rho_0 c_{p_{\mathrm{ref}}}}{k_{\mathrm{ref}}} \tag{3}$$

where L_{ref} and U_{ref} are select reference length and velocity scales respectively, ν_{ref} is the reference kinematic viscosity, $c_{p_{\mathrm{ref}}}$ is the reference specific heat, k_{ref} is the reference thermal conductivity, and ρ_0 is reference density.

Two 2D incompressible isothermal Navier-Stokes formulations are evaluated. The vorticity-streamfunction ($\omega - \psi$)-dependent variable transformation ensures continuity [19], hence for isothermal 2D flow,

$$q = \{\omega\} \qquad \text{and} \qquad q_a = \{\psi\} \tag{4}$$

The resultant forms for (1*a*) and (1*b*) are

$$\mathscr{L}(\omega) = \frac{\partial \omega}{\partial t} + u_j \frac{\partial \omega}{\partial x_j} - \frac{1}{\mathrm{Re}} \frac{\partial^2 \omega}{\partial x_j^2} = 0 \tag{5a}$$

$$\mathscr{L}_a(\psi) = -\frac{\partial^2 \psi}{\partial x_j^2} - \omega = 0 \tag{5b}$$

and the no-slip kinematic boundary condition constraint for ω is derived from (5*b*).

The second incompressible formulation is of "pressure relaxation" form, involving a constraint for continuity and a computation for genuine pressure [20]. The resultant state variable definition for isothermal flow is

$$q = \begin{Bmatrix} u_1 \\ u_2 \end{Bmatrix} \qquad \text{and} \qquad q_a = \begin{Bmatrix} \phi \\ P \end{Bmatrix} \tag{6}$$

where the forms for (1*b*) are

$$\mathscr{L}_a(\phi) = -\frac{\partial^2 \phi}{\partial x_i^2} - \frac{\partial \tilde{u}_i^{n+1}}{\partial x_i} = 0 \tag{7a}$$

$$\mathscr{L}_a(P) = -\frac{\partial^2 P}{\partial x_i^2} - s(q) = 0 \tag{7b}$$

Pure Neumann boundary conditions exist for both members of q_a, and during iteration, the approximation to the action of pressure is of the form

$$P^{n+1} \to P^* \approx P^n + \frac{1}{\theta \Delta t} \sum_i \phi^i \tag{8}$$

The discretely divergence-free velocity field thus attained is employed in evaluation of the source term in (7*b*).

THE FE WEAK STATEMENT FORMULATION

The three selected conservation law Navier-Stokes (NS) systems exhibit distinct formulational aspects. Independent of the specific form for q, f_j, f_j^v, and q_a in (1*a*)–(1*b*), spatial and temporal discretization of a Galerkin weak statement always produces a nonlinear algebraic statement. The finite-element (FE) spatial semidiscretization of the domain Ω of (1*a*)–(1*b*) employs the mesh $\Omega^h = \cup_e \Omega_e$, where Ω_e denotes the generic computational finite-element domain. Using superscript h to denote "spatial discretization," the FE approximation form for the state variables in (1*a*)–(1*b*)

$$q, q_a \approx q^h(\mathbf{x}, t) = \bigcup_e q_e(\mathbf{x}, t) \tag{9}$$

$$q_e(\mathbf{x}, t) = \{N_k(\mathbf{x})\}^T \{Q(t), QA(t)\}_e \tag{10}$$

where $\{\cdot\}$ denotes a column matrix, superscript T its transpose, and the FE basis set $\{N_k(\mathbf{x})\}$ contains Lagrange polynomials complete to kth degree. For example, the 1D Lagrange basis function sets for $1 \leqslant k \leqslant 3$ are

$$\{N_1\} = \begin{Bmatrix} 1-\zeta \\ \zeta \end{Bmatrix} \qquad \{N_2\} = \begin{Bmatrix} (1-\zeta)(1-2\zeta) \\ 4(1-\zeta)\zeta \\ \zeta(2\zeta - 1) \end{Bmatrix}$$

$$\times \{N_3\} = \tfrac{9}{2} \begin{Bmatrix} (1-\zeta)\left(\zeta^2 - \zeta + \frac{2}{9}\right) \\ (1-\zeta)\zeta(2-3\zeta) \\ (1-\zeta)\zeta(3\zeta - 1) \\ \zeta\left(\zeta^2 - \zeta + \frac{2}{9}\right) \end{Bmatrix} \tag{11}$$

where $\zeta(x) = (1 + \eta)/2$ and $\eta : (-1, 1)$ is the local normalized natural coordinate. The d-dimensional forms and extensions are well known; cf. [15].

The spatially discrete FE evaluation of the *Galerkin weak statement* GWS^h for $(1a)$ leads to the form

$$\text{GWS}^h = S_e\left(\int_{\Omega^h}\{N_k\}\left[\frac{\partial q^h}{\partial t} + \frac{\partial}{\partial x_j}(\mathbf{f}_j - \mathbf{f}_j^v)^h - s\right]d\tau\right) \equiv \{0\} \tag{12a}$$

$$= S_e\left(\int_{\Omega^h}\{N_k\}\left(\frac{\partial q^h}{\partial t} - s\right)d\tau - \int_{\Omega^h}\frac{\partial\{N_k\}}{\partial x_j}(\mathbf{f}_j - \mathbf{f}_j^v)^h\,d\tau \right.$$

$$\left. + \oint_{\partial\Omega_e\cap\partial\Omega^h}\{N_k\}(\mathbf{f}_j - \mathbf{f}_j^v)^h\hat{n}_j\,d\sigma\right) \tag{12b}$$

where the Green-Gauss divergence theorem exposes the indicated boundary fluxes on $\partial\Omega^h$, S_e symbolizes the "assembly operator" carrying local (element) matrix coefficients into the global arrays, and $d\tau$ and $d\sigma$ denote differential elements on Ω and $\partial\Omega$, respectively. The surface integrals in $(12b)$ contain unknown boundary fluxes wherever Dirichlet (fixed) boundary conditions are enforced.

The companion *Taylor weak statement* TWS^h [1] extended to system $(1a)$, under certain simplifications, yields the modified form

$$\mathscr{L}^c(q) = \mathscr{L}(q) = \beta\,\Delta t\,\frac{\partial}{\partial x_j}\left(A_j A_k\,\frac{\partial q}{\partial x_k}\right) = 0 \tag{13}$$

where $A_j = \partial f_j/\partial q$ is the kinetic flux vector Jacobian and β is a parameter eligible for optimization [1]. Independent of the dimension d of Ω, and for general forms of the flux vectors, GWS^h in $(12a)$ always produces a nodal-order (large) ordinary differential equation (ODE) system of the form

$$\text{GWS}^h = [M]\,\frac{d\{Q(t)\}}{dt} + \{R(Q)\} = \{0\} \tag{14}$$

where $d\{Q\}/dt \equiv \{Q\}'$ vanishes at steady state. The system square matrix $[M]$ and residual column matrix $\{RQ\}$ are formed via assembly over $\Omega^h = \cup\,\Omega_e$ of corresponding element rank matrices, i.e.,

$$[M] = S_e[M_k]_e \qquad \text{and} \qquad \{R(Q)\} = S_e\{R_k(Q)\}_e \tag{15}$$

where subscript k in (15) emphasizes dependence on FE basis degree k in (10).

The form (14) provides the statement of local time derivative necessary to evaluate a temporal Taylor series. For example, selecting the θ-implicit one-step Euler family,

$$\{Q(t_{n+1})\} \equiv \{Q\}_{n+1} = \{Q\}_n + \Delta t[\theta\{Q\}'_{n+1} + (1 - \theta)\{Q\}'_n] + \mathscr{O}(\Delta t^{f(\theta)})$$

$$= \{Q\}_n - \Delta t[M]^{-1}(\theta\{R\}_{n+1} + (1 - \theta)\{R\}_n) \tag{16}$$

where subscript n denotes discrete time level. Clearing $[M]^{-1}$ and collecting terms to a homogeneous form yields the WS^h + θTS algorithm terminal algebraic form,

$$\{FQ\} = [M]\{Q_{n+1} - Q_n\} + \Delta t(\theta\{R\}_{n+1} + (1 - \theta)\{R\}_n) = \{0\} \tag{17}$$

The discrete Galerkin weak statement for (1b) produces a companion matrix system,

$$\{FQA\} = [D]\{Q_a\} - \{S(Q)\} = \{0\} \tag{18}$$

where the symmetric square matrix $[D]$ is the discrete Laplacian, $\{Q_a\}$ is the nodal array of q_a^h, and $\{S(Q)\}$ contains dependence on q^h via solution $\{Q(t)\}$ from (17).

The *Newton algorithm* for solution of (17) is

$$[\text{JAC}]\{\delta Q\}^{p+1} = -\{FQ\}_{n+1}^p \tag{19}$$

where, for iteration index p,

$$\{Q\}_{n+1}^{p+1} \equiv \{Q\}_{n+1}^p + \{\delta Q\}^{p+1} = \{Q\}_n + \sum_{i=1}^{p} \{\delta Q\}^{i+1} \tag{20}$$

and the Newton *Jacobian* definition is

$$[\text{JAC}] = \frac{\partial\{FQ\}}{\partial\{Q\}} = [M] + \theta\Delta t\left(\frac{\partial\{R\}}{\partial\{Q\}}\right) \qquad \frac{\partial\{FQA\}}{\partial\{QA\}} = [D] \tag{21}$$

THE SGM FINITE ELEMENT

The SGM element construction for a 1D scalar model of (1a) leading to a theoretical *nonlinear* monotonicity constraint via enforcement of a real eigenvalue spectrum for the GWS^h algorithm recursion stencil is detailed in [15]. The nonlinear extension of this theory leads to prediction of an optimal distribution of the SGM embedded parameter (sets) on each element, hence over the mesh Ω^h. The theoretical generalization to nonuniform, d-dimensional discretizations leads to some issues still requiring resolution, to fully achieve the potential for attainment of nodally accurate monotone solutions on arbitrary d-dimensional meshes.

The global assembly of the element canonical form of the diffusion matrix $[D]_e$ resembles an identity matrix, *excellent* for numerical computation independent of the basis degree k ([18], sec 5.5). Conversely, the assembly of the element canonical convection matrix $[U]_e$ always yields a null matrix. In addition, in higher dimensions, the matrix $[U]_e$ cannot be statically condensed, as the convective information contained at element mid-side nodes may not be eliminated. Hence, contrary to the convective flux vector manipulation as a stability-enhancement approach, the SGM element procedure is restricted to the diffusion matrix resulting from f_j^v [18].

The 1D Lagrange linear ($k = 1$) and quadratic ($k = 2$) FE basis polynomial set, the $k = 1$, $p = 2$ hierarchical (bubble) element, and the SGM $S = 2$ ($k = 2$,

reduced) Lagrange element for one dimension are compared in Figures 2*a*–2*d*. Both the Lagrange $k = 2$ and p-hierarchical elements contain an extra degree of freedom (node **2** in Figures 2*b* and 2*c*). For the SGM element, the explicit appearance of the embedded degree of freedom is eliminated via static condensation [15].

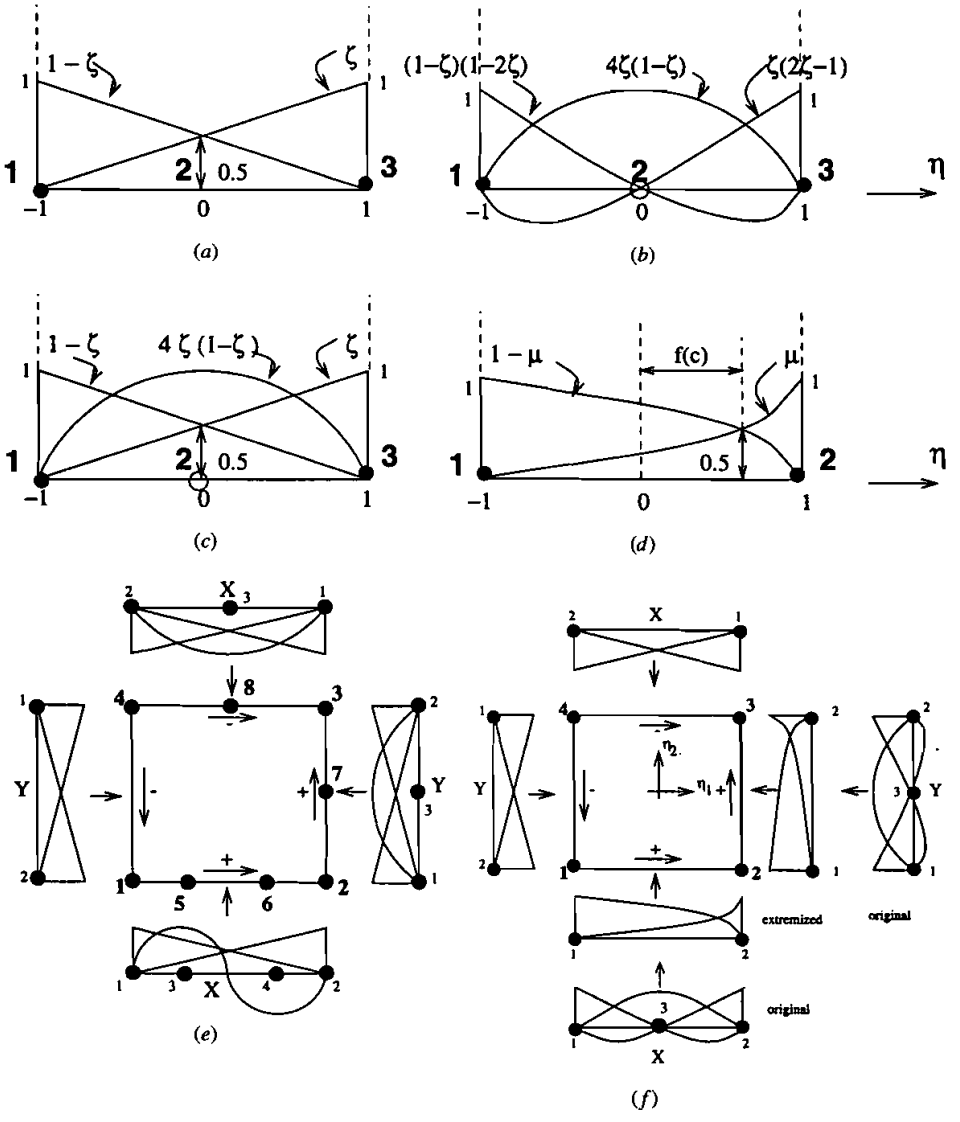

Figure 2. Comparison of standard, hierarchical, SGM elements in one and two dimensions. (*a*) 1-D Lagrange element, $k = 1$; (*b*) 1-D Lagrange element, $k = 2$; (*c*) 1-D hierarchical element, $k = 1$, $p = 2$; (*d*) 1-D SGM Lagrange element, k^2, reduced; (*e*) 2-D hierarchical element, $k = 1, 2, 3$ selectively; (*f*) 2-D SGM element, $S = 2$.

For the linear dissipative flux vector FE construction, static condensation of any $k > 1$ basis Lagrange element in one dimension simply returns the $k = 1$ form [15]. Therefore, the SGM theory augments the diffusion matrix via an *embedding* function $g(x, c)$, hence the name "SubGrid eMbedded." The definite integral form of the SGM basis function set, denoted $\{N_S\}$, for $[D]_e$ in (15) is

$$\int_{\Omega_e} \frac{\partial\{N_S\}}{\partial x} \frac{\partial\{N_S\}^T}{\partial x} dx \equiv \int_{\Omega_e} g(x,c) \frac{\partial\{N_k\}}{\partial x} \frac{\partial\{N_k\}^T}{\partial x} dx \Big|^R \tag{22}$$

where the statically condensed, reduced Rank form is denoted as $|^R$. The embedded polynomial $g(x, c)$ contains one arbitrary parameter c for each additional Lagrange degree $k \geq 2$. The form of the 1D SGM element basis set $\{N_S\}$ for $k = 2 = S$ is expressed, analogous to the $k = 1$ Lagrange basis, (11), as

$$\{N_S\} = \begin{Bmatrix} 1 - \mu \\ \mu \end{Bmatrix} \tag{23}$$

where $\mu = \sum_{i=1}^{\infty} a_i \zeta_i^{\alpha}$ is a polynomial function of an expansion coefficient set, a_i, dependent on embedding degree k, and the $k = 1$ local coordinate ζ, and α is a function of c. A detailed computation of the SGM 1D basis is provided in [15].

If the embedded polynomial in (22) is selected as quadratic, then $g_2 = \{1, c, 1\}\{N_2\}$, where $\{N_2\}$ is the Lagrange quadratic basis. Then, for $S = 2 = k$, the 3×3 element matrix form for $[D]_e$ prior to condensation is

$$[D_{k=2}]_e = \frac{1}{15h_e} \begin{bmatrix} (18c + 17) & (7 - 2c) & -(16c + 24) \\ (7 - 2c) & (18c + 17) & -(16c + 24) \\ -(16c + 24) & -(16c + 24) & (32c + 48) \end{bmatrix} \tag{24}$$

Static condensation of this matrix yields

$$[D_{k=2}]_e^R \Rightarrow [D_{S=2}]_e = \frac{1}{3h_e} \begin{bmatrix} (2c + 1) & -(2c + 1) \\ -(2c + 1) & (2c + 1) \end{bmatrix} \tag{25}$$

The discussion in [15] (Appendix B) confirms that $c \geq 1$ is the requirement. For $c \equiv 1$, $[D_{S=2}]_e$ in (25) is identical to the linear Lagrange matrix,

$$[D_{k=1}]_e = \frac{1}{h_e} \begin{bmatrix} 1 & -1 \\ -1 & 1 \end{bmatrix}$$

This degeneracy is termed *consistent*, which occurs only for $d = 1$. Specifically, for $d > 1$ dimensions, static condensation of a $k > 1$ diffusion matrix does not yield the $k = 1$ form.

The d-dimensional form in the dissipative flux vector diffusion matrix $[D]_e$ in (11), formed via the SGM element (denoted by subscript S), is

$$[D_S]_e \equiv \int_{\Omega_e} g(\mathbf{x}, \mathbf{c}) \frac{\partial\{N_k\}}{\partial \mathbf{x}} \frac{\partial\{N_k\}^T}{\partial \mathbf{x}} d\tau \Bigg|^R \tag{26}$$

$$= \int_{\Omega_e} \frac{\partial\{N_S\}}{\partial \mathbf{x}} \frac{\partial\{N_S\}^T}{\partial \mathbf{x}} d\tau \tag{27}$$

and many selections are possible. For $d \geqslant 1$, $g_2(\mathbf{x}, \mathbf{c})$ is written as

$$g_2 = \{G\}_e^T \{N_2\} \tag{28}$$

For the $d = 2$ vector $\mathbf{c} = (c_x, c_y)$, the element array is $\{G\}_e^T = \{1, 1, 1, 1, c_x, c_y, c_x, c_y, c_x c_y\}$ and $\{N_2\}$ is the corresponding Lagrange quadratic basis set. The array $\{G\}_e$ may be represented by the matrix outer product

$$\{G\}^T \Rightarrow \{1, c_x, 1\} \otimes \{1, c_y, 1\} \tag{29}$$

which is pictured as the tensor product $A \otimes B$ of $A = \{1, c_x, 1\}$ and $B = \{1, c_y, 1\}$, that is,

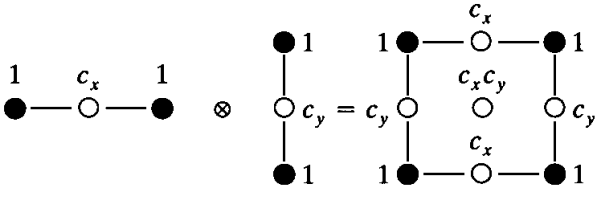

The $d = 3$ extension is obvious. Element constructions for $d = 2$ are illustrated in Figures 2e–2f. Figure 2e graphs a p-hierarchical 2D element with two quadratic sides ($p = 2$), one cubic side ($p = 3$), and a linear side. The $k = 2$ ($S = 2$) condensed 2D SGM element, graphed in Figure 2f, is very distinct from both the p-element and the Lagrange $k = 2$ element.

The diffusive flux vector matrix $[D]_e$ in (11), formed with the Lagrange bilinear ($k = 1$) basis in two dimensions for a generic cartesian element of unit span is

$$[D_1]_e = \int_{\Omega_e} \frac{\partial\{N_1\}}{\partial x_j} \frac{\partial\{N_1\}^T}{\partial x_j} d\tau = \frac{\det_e}{6} \begin{bmatrix} 4 & -1 & -2 & -1 \\ -1 & 4 & -1 & -2 \\ -2 & -1 & 4 & -1 \\ -1 & -2 & -1 & 4 \end{bmatrix} \tag{30}$$

where $\det_e$ is the transformation matrix determinant, equal to one-fourth the plane area of Ω_e. The $S = 2$ extremized form for (26) for two dimensions is constructed

as

$$[D_S]_e = \frac{\det_e}{6}\begin{bmatrix} d_{11} & d_{12} & d_{13} & d_{14} \\ d_{21} & d_{22} & d_{23} & d_{24} \\ d_{31} & d_{32} & d_{33} & d_{34} \\ d_{41} & d_{42} & d_{43} & d_{44} \end{bmatrix} \tag{31}$$

where each matrix element d_{ij} in (31) is a distinct polynomial function of c_x and c_y [18]. For example, assuming that $c_x = c = c_y$, the first term in (31) becomes

$$d_{11} = \frac{2c + 1}{15(148c^2 + 164c + 73)}(656c^3 + 2{,}032c^2 + 1{,}838c + 549) \tag{32}$$

Simplifying further to $c_x = c_y = c = 1$, the $S = 2$ SGM diffusion matrix form is

$$[D_S]_e = \frac{\det_e}{66}\begin{bmatrix} 29 & -11 & -7 & -11 \\ -11 & 29 & -11 & -7 \\ -7 & -11 & 29 & -11 \\ -11 & -7 & -11 & 29 \end{bmatrix} \tag{33}$$

The distinctions between (30) and (33) are apparent.

For general applications, a nodally distributed (subscript j) SGM parameter is preferable to an element parameter. Therefore, defining $r_j = (2c_j + 1)/3$, the monotonicity constraint form becomes

$$\frac{2c_j + 1}{3} \equiv r_j \geqslant \frac{|u_j|h_j}{\epsilon\mathscr{F}} = \frac{|u_j|h_j\,\mathrm{Re}}{\mathscr{F}} \tag{34}$$

where Reynolds number Re replaces ϵ and $\mathscr{F} > 0$ is a real number. In one dimension, $\mathscr{F}$ is precisely determined from the eigenvalue analysis, hence $\mathscr{F} = 2$ for the linear convection-diffusion (Peclet) problem, $\mathscr{F} = 6$ for the linear stationary wave definition, while $\mathscr{F} = 3$ for the nonlinear convection-diffusion (viscous Burgers) equation [15]. However, for multidimensional problems, determining a suitable functional form for $\mathscr{F}$ involves definition of a correlation function $\mathscr{F}_{ij} = f(\mathrm{Re}, \det_e)$, the form of which must be validated.

For velocity field $\mathbf{u}_j = (u_{1j}, u_{2j}, u_{3j})$, principal coordinate mesh measures h_{1j}, h_{2j}, and h_{3j}, and principal coordinate diffusion parameter set $\epsilon_j \Rightarrow (\epsilon_{1j}, \epsilon_{2j}, \epsilon_{3j})$, the condition for a d-dimensional monotone solution is expressed for scalar components of $\mathbf{r}_j = (r_{1j}, r_{2j}, r_{3j})$ in (29), and this correlation function $\mathscr{F}_{ij}$ is

$$r_{ij} \geqslant \frac{|u_{ij}|h_{ij}}{\mathscr{F}_{ij}\epsilon_{ij}} \qquad \text{where } \mathscr{F}_{ij} = \left(\frac{AV_e}{\epsilon_{ij}^{d-1}h_{ij}}\right)^{1/d}, 1 \leqslant i \leqslant d, \text{ and } 1 \leqslant j \leqslant N \text{ node} \tag{35}$$

Hence, only the scalar $0 < A < 2$ remains undefined, and must be estimated. V_e $(= 2^d \det_e)$ is the volume (area) of the d-dimensional element, and the form for $\mathscr{F}_{ij}$ was determined using computational data from the 2D and 3D linear Peclet problem solutions [15].

The steps forming the SGM element GWS^h solution process include:

1. Use the monotonicity constraint (34)–(35) to compute c_j or r_j, or estimate $r_{ij} = f(u_j, h_j, \text{Re})$. For the node where r_j, r_{ij}, $c_j < 1$, the value is obtained as the average from neighboring nodes.
2. Form

$$[D]_e = \int_{\Omega_e} g_2(\mathbf{c}) \frac{\partial \{N_S\}^T}{\partial x_j} \frac{\partial \{N_S\}^T}{\partial x_j} d\tau$$

   where $g_2(\mathbf{c}) = \{G\}^T\{N_2\}$.
3. Rank reduce $[D]_e$ to $[D_S]_e$ via static condensation.
4. Form the weak statement WS^h (17)–(21) for the discretized domain $\Omega^h \bigcup_e \Omega_e$.
5. Solve (19).
6. Return to step 1 and repeat the process until solution is converged.

RESULTS AND DISCUSSION

Computational results verifying theory and summarizing performance for select Navier-Stokes problem statements are presented. The problem domains lie on $\Re^d$ for $d = 1, 2$ in $(1a)$–$(1b)$, with the SGM element appropriately formed. Steady-state solutions of the Navier-Stokes equations $(1a)$–$(1b)$ for quasi-1D compressible de Laval nozzle shock, 2D incompressible flow in a shear-driven cavity, and 2D incompressible flow over a backward-facing step duct document application of the SGM element.

A traditional measure for estimating semidiscrete approximation error, $e^h = q - q^h$, is the L_2 "energy seminorm" $\|\cdot\|_E$, defined as

$$\|q^h\|_E \equiv 0.5 \int_\Omega \frac{\partial q^h}{\partial x_j} \epsilon \frac{\partial q^h}{\partial x_j} d\tau \qquad \text{for } 1 \leqslant j \leqslant d \tag{36}$$

where ϵ remains the diffusion coefficient in the dissipative flux vector in $(1a)$.

For a 1D axisymmetric steady conduction problem, the g_1 embedding and $S \geqslant 2$ SGM element solution convergence rate is documented in [15]; c.f. Figure 3. The slope of the convergence rate increases rapidly as S increases. Specifically, for $S = 4$, the convergence data are interpolated by a line of slope 12.6, which exceeds the classical $k = 4$ slope of 8. It is also noted in [15] that for 1D linear and nonlinear convection-diffusion problem, the g_2 embedding and $S = 2$ SGM element "solutions exhibit no convergence rate, since the solution is nodally exact" for the computed value of c_j or r_j via (34). However, the solution energy norm may overshoot or undershoot for an overprediction or underprediction of c_j or r_j.

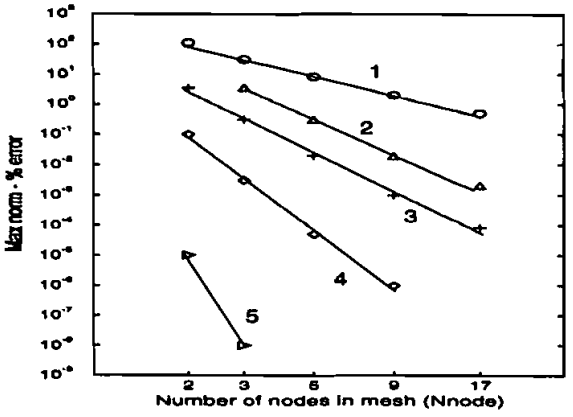

(*a*)

line no.	*k*	*S*	slope
1	1	0	2.0
2	2	0	4.0
3	0	2	4.5
4	0	3	6.2
5	0	4	10.8

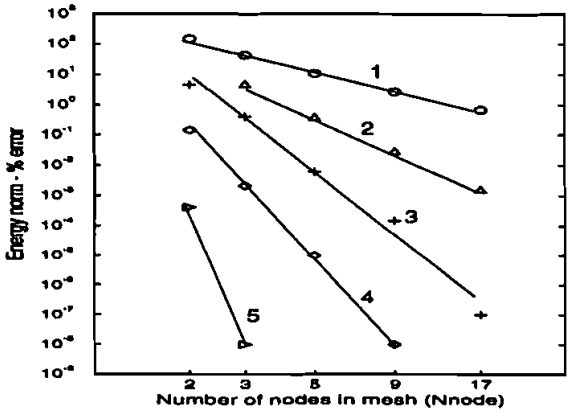

(*b*)

line no.	*k*	*S*	slope
1	1	0	2.0
2	2	0	4.0
3	0	2	5.5
4	0	3	6.9
5	0	4	12.6

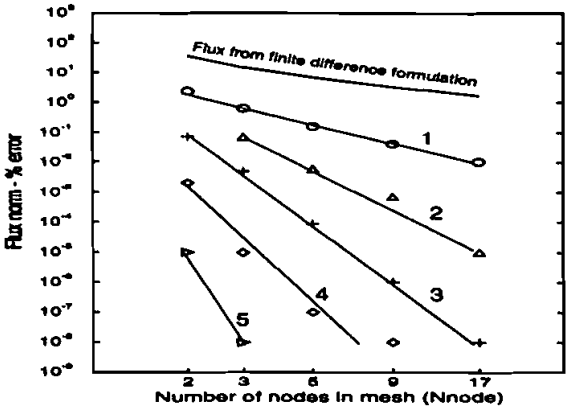

(*c*)

Flux from Weak Statement

line no.	*k*	*S*	slope
1	1	0	2.0
2	2	0	4.0
3	0	2	5.3
4	0	3	6.5
5	0	4	10.0

Figure 3. Convergence study for 1D steady heat conduction problem [15]. (*a*) Max norm; (*b*) energy norm; (*c*) boundary flux point.

Quasi-1D Compressible de Laval Nozzle Shock Verification

The quasi-1D compressible Navier-Stokes form is stated in (2*a*)–(2*b*). The normalized variable crossection A is defined for a de Laval nozzle geometry, Figure 4*a*, using the problem specification of [21], that is,

$$A(x) = \begin{cases} 1.75 - 0.75\cos[2(x - 0.5)\pi] & 0.0 \leqslant x \leqslant 0.5 \\ 1.25 - 0.25\cos[2(x - 0.5)\pi] & 0.5 \leqslant x \leqslant 1.0 \end{cases} \tag{37}$$

The nondimensional initial condition for state variable q is the sonic throat, shock-free isentropic solution for (37). The reference state is inflow, hence the boundary conditions are $\rho(0,t) = 1.0 = \rho_{\text{in}}$, $E(0,t) = 1.0 = E_{\text{in}}$, and $p(1,t) = p_{\text{out}} = 0.909$. The corresponding inlet Mach number is $\text{Ma}_{\text{in}} = 0.2395$.

The verification problem definition is the steady state following an impulsive change from isentropic flow by decreasing the exit pressure p_{out} from 0.909 to 0.864. The resultant expansion wave propagates upstream to the throat, hence triggers formation of a (normal) shock that moves downstream. The analytical solution shock is located at $x = 0.65$ and the shock Mach number is $\text{Ma}_s = 1.37$. First, the nozzle domain is uniformly discretized into 50 elements. The nondissipative GWS algorithm solution diverges for this problem. The TWS dissipative algorithm for $\beta \Rightarrow \beta_q = 0.1$–$0.2$ converges to a steady state with shock location and sharpness, hence nonmonotone character, as a function of β, Figure 4*b*. A close look near the shock region reveals that the TWS $\beta = 0.2$ solution is substantially diffused, while the $\beta = 0.1$ solution is nonmonotone (oscillatory). The SGM solution Mach number distribution for $\mathcal{F}_p = 9$, $\mathcal{F}_E = 10$, $\mathcal{F}_m = 12.0$ at $\text{Re} = 10^6$ is also plotted in Figure 4*b* It is monotone and follows the analytical solution more closely than either TWS solution. Figure 4*c* verifies the monotonicity of the SGM solution during time evolution to steady state. Finally, the SGM solution on a modestly nonuniform 50-element mesh is monotone and accurately captures the steady-state shock across two nodes at Ma = 1.369 and 0.78, Figure 4*d*. The analytical solution is also plotted for comparison, documenting that this nonuniform mesh SGM solution is essentially the Lagrange interpolant of the exact solution. The iteratively determined SGM parameter set, as determined via (35) and the distributed rsgm_q, is plotted in Figure 4*e*. For $\text{Re} = 10^6$, the parameters range between 10^3 and 10^4, and a very sharp shock point operator is confirmed present.

Shear-Driven Cavity Flow

The laminar flow of an incompressible fluid in a square cavity with the top lid translating at constant velocity in its own plane is a standard benchmark problem. Despite the boundary condition singularities at the two corners, for moderately high values of the Reynolds number Re, published comparative results of accepted accuracy are available (cf., [22]–[25]) on moderate to very dense meshes. For example, [25] used a 51×51 uniform mesh for a least-squares finite-element

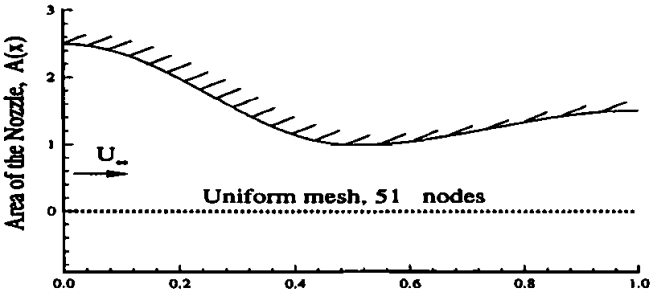

(*a*)

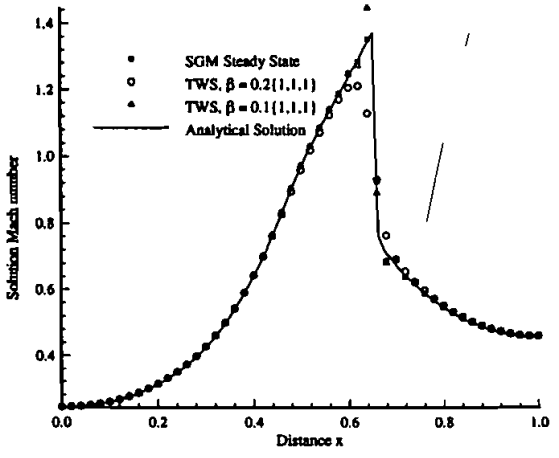

(*b*)

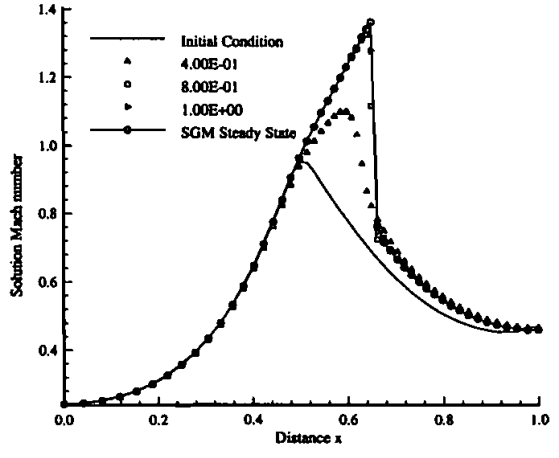

(*c*)

Figure 4. Steady-state solution Ma and rsgm_q distribution for compressible flow, Re = 10^6. (*a*) de Laval nozzle geometry; (*b*) TWS and SGM comparison on uniform mesh; (*c*) time evolution of SGM solution.

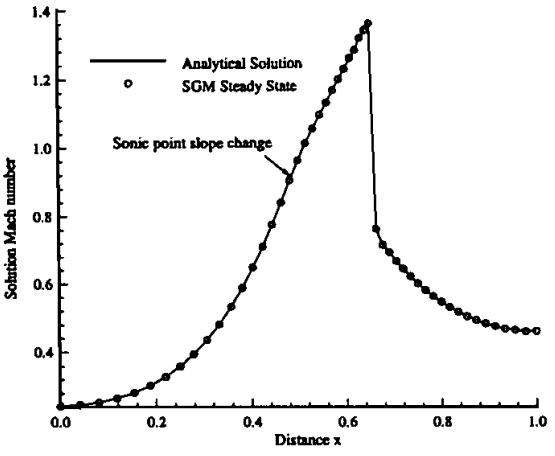

(*d*)

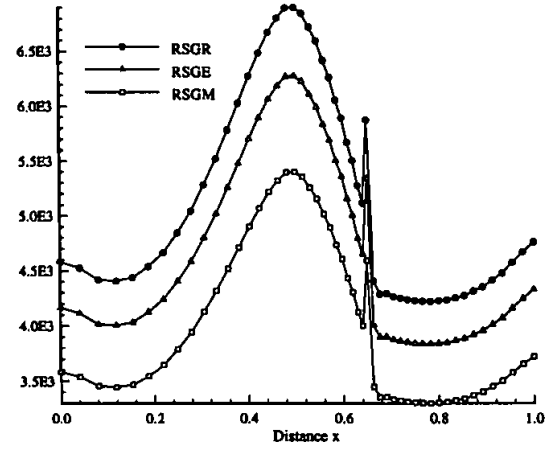

(*e*)

Figure 4. Steady-state solution Ma and rsgm_q distribution for compressible flow, Re = 10^6 (*Continued*). (*d*) SGM solution on 51-node nonuniform mesh; (*e*) steady-state distributed SGM parameter rsgm_q.

method (LSFEM) solution, while [22] employed up to a 257 × 257 uniform mesh via a multigrid approach for 100 ⩽ Re ⩽ 10,000. For Re ⩽ 100, all results agree well, indicating that coarser grids usually employed by practitioners are adequate. As Re increases, however, coarse mesh inadequacy becomes fully apparent. This is particularly evident in the solutions reported in [23]. Nevertheless, the fourth-order-accurate spline method [24] solution remains satisfactory computed on a 17 × 17 mesh at Re = 1,000, but "the corresponding computer time becomes large."

The driven-cavity problem, via the vorticity-streamfunction form (5*a*)–(5*b*), was studied using GWS^h and SGM^h algorithms for $100 \leqslant \mathrm{Re} \leqslant 3{,}200$ on coarse (17×17) to moderately dense (65×65) meshes [18]. The solution comparisons are documented here for Re = 3,200 computed on nonuniform meshings. Figure 5 compares two GWS^h and SGM^h vorticity solution distributions in perspective with corresponding 17×17 meshes overlaid. (Color figures are available for Figures 5–8 and Figures 12–14 at http://cfdlab.engr.utk.edu/html/SGM/index.html.) The GWS^h vorticity solution, Figure 5*a*, is totally polluted by a mesh-scale dispersive error oscillation near the moving lid. The companion SGM^h vorticity

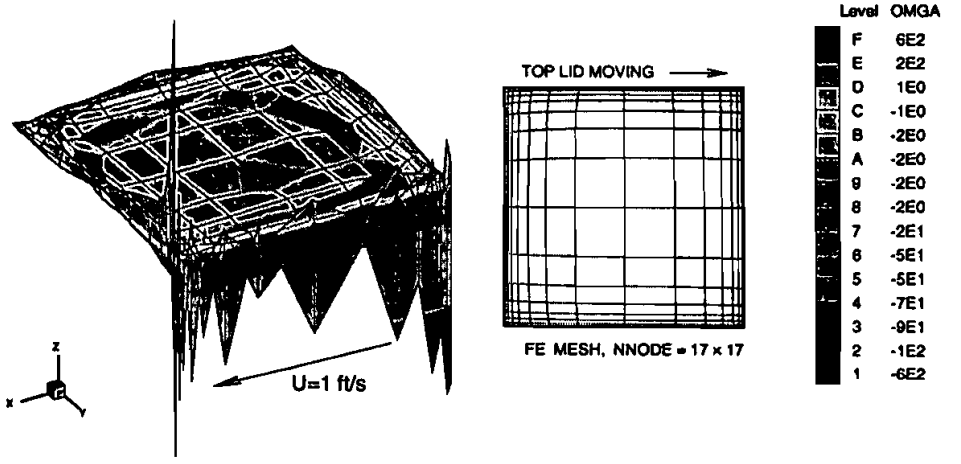

(*a*)

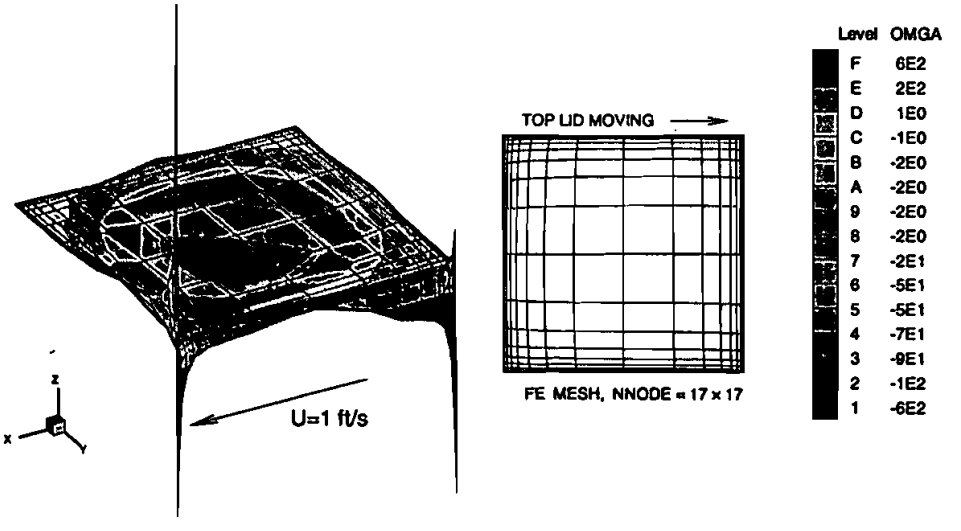

(*b*)

Figure 5. GWS^h (*a*) and SGM^h (*b*) vorticity solution comparison for driven cavity (Re = 3,200; $\beta = 0.0$).

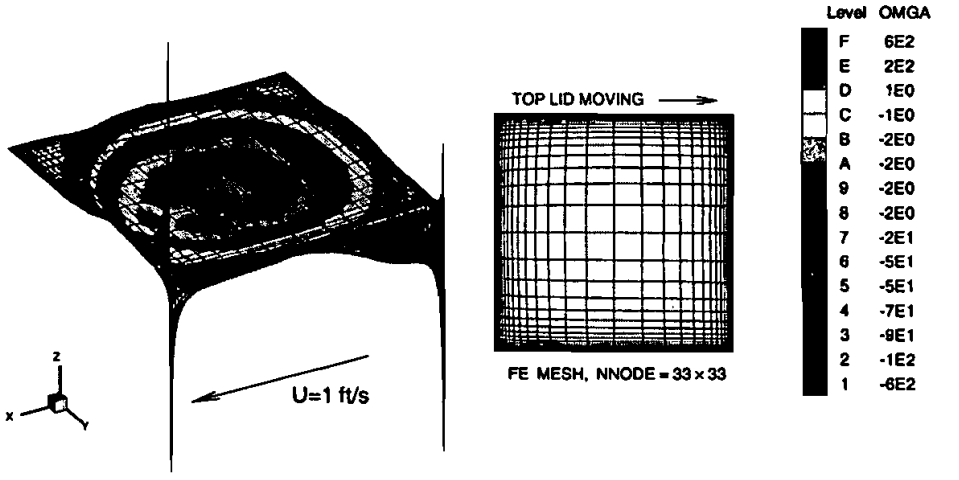

(*c*)

Figure 5. GWS^h (*Continued*). (*c*) Vorticity solution comparison for driven cavity (Re = 3,200; $\beta = 0.0$).

solution, obtained with optimal nodally distributed parameter $\text{rsgm}_j \geqslant 1$ on the identical nonuniform 17 × 17 mesh, Figure 5*b*, verifies attainment of a monotone solution exhibiting very sharp corner (singularity) extrema. This solution resolution is comparable to that obtained via the GWS^h algorithm on a double-density (33 × 33), highly nonuniform mesh, Figure 5*c*. While neither was optimized, the Newton algorithm computation time for the GWS^h solution was nearly six times that required for the SGM^h solution, Figure 5*b*, and the memory requirement was four times larger.

The accuracy comparisons to benchmark data for the 33 × 33 GWS^h solution is essentially identical to the 17 × 17 SGM^h solution summarized in Figure 6. The normal arrowheads on each secondary vortex region graph locate the attachment points documented in [22], Figure 3, on a 129 × 129 uniform mesh; the nonuniform 17 × 17 SGM solution agreement is excellent. The SGM solution u- and v-velocity profiles through the geometric center, Figure 6, also agree within ~ 1% with those generated by the 57 times denser mesh solution of [22], Figures 2*a* and 2*b*, as documented by the circles in Figure 6.

Pressure prediction is a postprocessing operation with a vorticity-streamfunction algorithm solution [20, 26] via solving a Poisson equation with source (the nonlinear product of velocity derivatives). Pressure distributions computed from the 17^2 and 33^2 GWS^h solutions, and the 17^2 SGM^h solution, are compared in Figure 7. The SGM^h solution clearly exhibits the "best" local extrema prediction. However, an adverse effect of the coarse centroidal region mesh is also apparent; compare Figures 7*b* and 7*c*.

The nonlinearly computed nodal distributions of the SGM^h theory parameter sets RSGM_x and RSGM_y are graphed in perspective in Figures 8*a* and 8*b*. To assist in visualizing these data, the local u, v velocity scales are employed as the

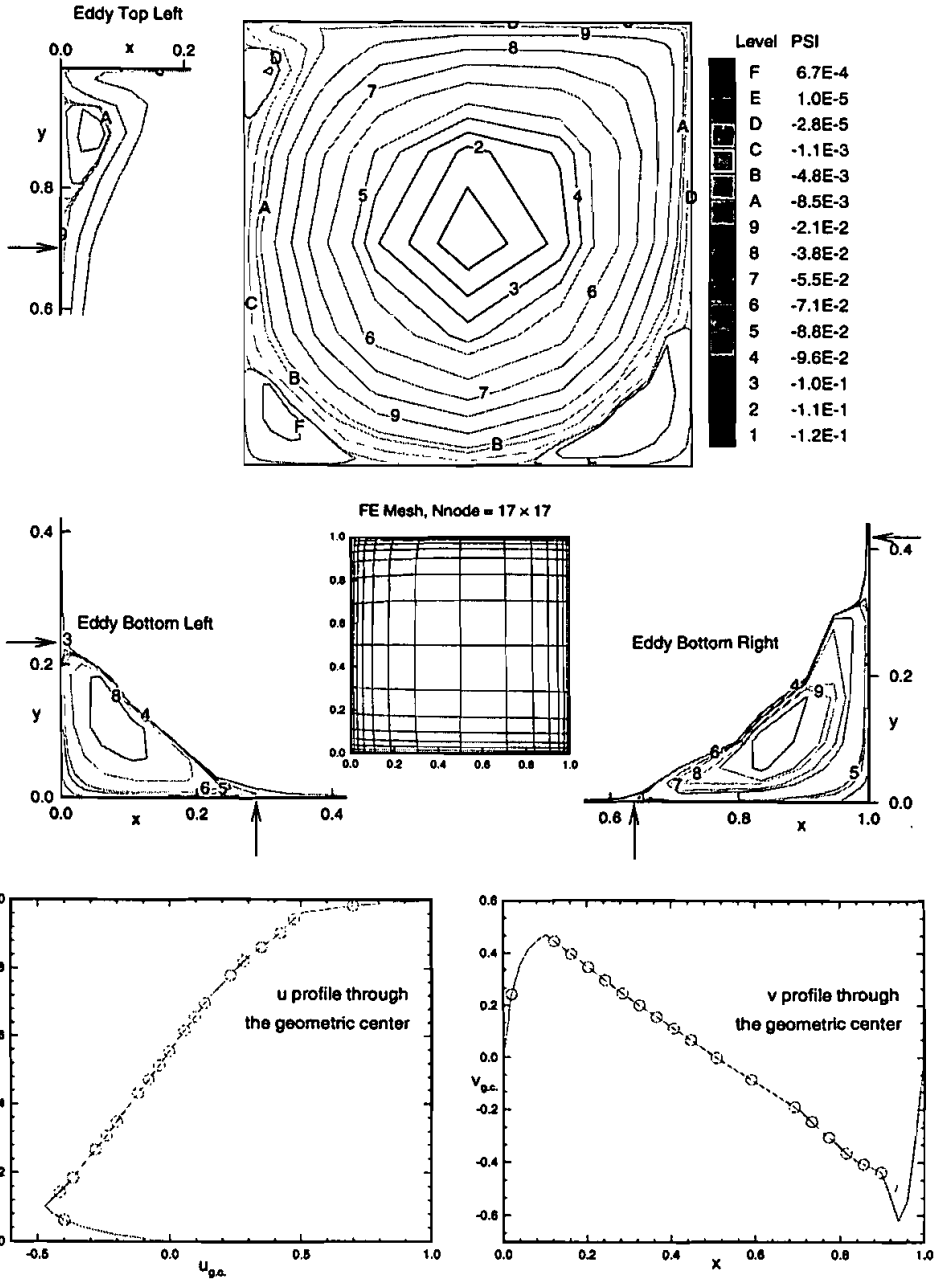

Figure 6. SGM^h streamfunction and velocity solution details for driven cavity, Re = 3,200, $\text{rsgm}_i \geqslant 1$.

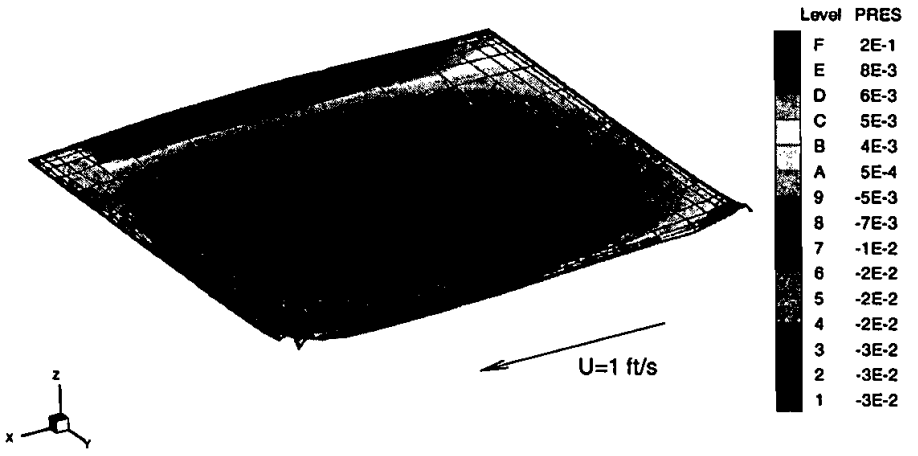

(*a*)

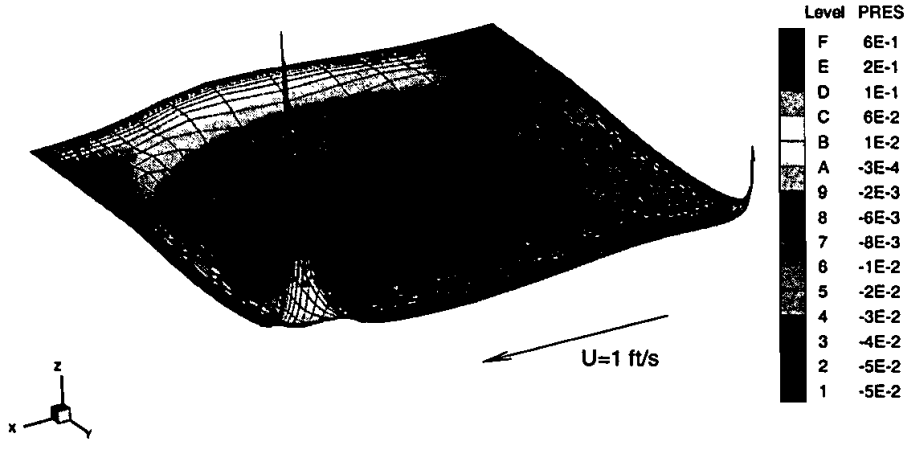

(*b*)

Figure 7. GWS^h and SGM^h comparison pressure solutions for driven cavity (Re = 3,200). (*a*) GWS^h on 289-node mesh; (*b*) GWS^h on 1089-node mesh.

elevation (z) reference. These distributions clearly indicate that the highest-level RSGM$_x$ (RSGM$_y$) is computed where the scalar magnitude of u (v) is the highest, and these data range (1, 9) and (1, 13) for this nonuniform meshing.

Close-Coupled Step Wall Diffuser

This 2D benchmark geometry has been widely studied [27–30], specifically for the wide, close-coupled geometry of [27], reporting laser-Doppler anemometer measurements of velocity distribution and separation region attachment intercepts. These data, for laminar, transitional, and turbulent flow measurements in air for

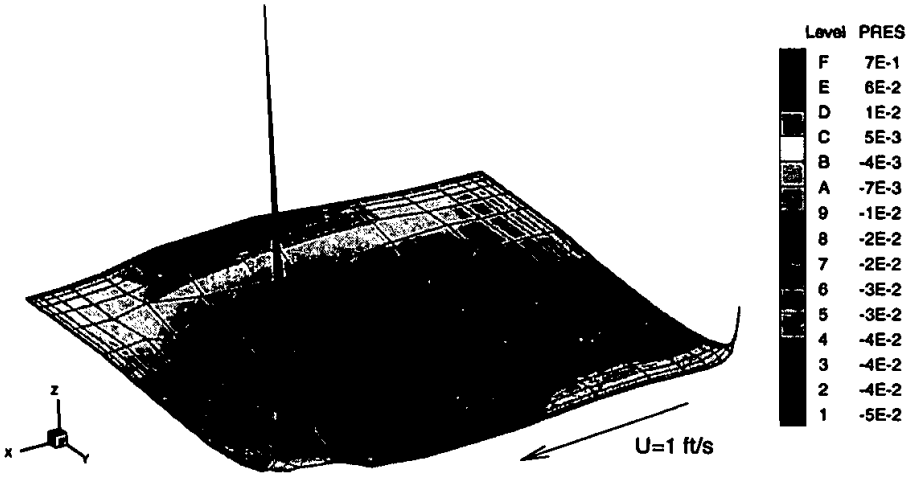

(*c*)

Figure 7. GWS^h and SGM^h comparison pressure solutions for driven cavity (Re = 3,200) (*Continued*). (*c*) SGM^h on 289-node mesh, $\text{rsgm}_i \geq 1.0$.

$70 < \text{Re} < 8{,}000$, confirm that the flow downstream of the step is essentially two-dimensional only for $\text{Re} < 400$, and becomes fully turbulent and returns to essential two-dimensionality for $\text{Re} > 6{,}500$.

Available fully 3D computational data for this geometry [20] predict that the three-dimensionality for $400 \leqslant \text{Re} \leqslant 800$ is confined mainly to the lateral sidewall regions, while the symmetry center plane flow field exhibits an essential two-dimensionality (as the normal velocity component vanishes). In both two and three dimensions, dispersion error control plays a critical role in maintaining CFD solution process stability for $\text{Re} > 400$. Prior to these data, [28] conjectured that the "abrupt change" in the flow structure from 2D to 3D flow was due to a Taylor-Görtler vortex instability that caused spanwise-periodic counterrotating vortex pairs aligned with the duct axis.

The fully 3D CFD solutions for $100 \leqslant \text{Re} \leqslant 800$, [20], refute this conjecture; i.e., the flow field transition to three dimensions proceeds smoothly for $\text{Re} > 400$. In either two or three dimensions, as the Reynolds number increases, the solution process becomes very sensitive to mesh resolution, hence stability, even using a Re continuation procedure, i.e., using the lower Re solution as the initial condition. The resultant instability in the GWS^h algorithm flow field prediction in three dimensions on an inadequate mesh was observed as periodic generation/annihilation of the secondary vortex structure (x_4 to x_5) along the top wall [20].

Therefore, a critical validation assessment in two dimensions is to predict the laminar flow solution at Re = 800, which according to experiment and the 3D computational solution, exhibits a steady state. There has existed some controversy regarding the CFD existence of a 2D steady-state; recently, a quadratic basis GWS^h algorithm on a dense mesh [30] confirmed that the steady solution was stable. The GWS^h, TWS^h, and SGM^h algorithms were implemented for the

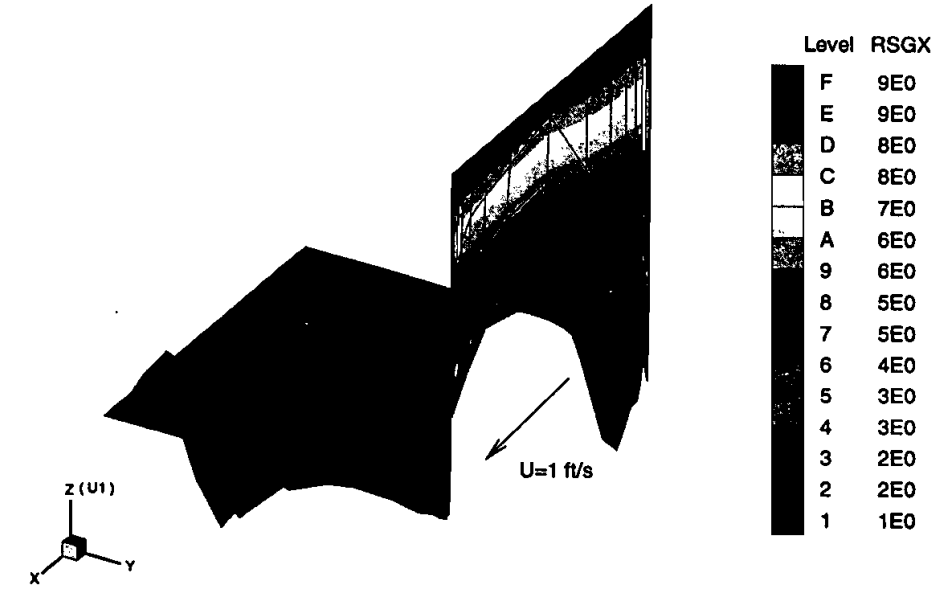

(*a*)

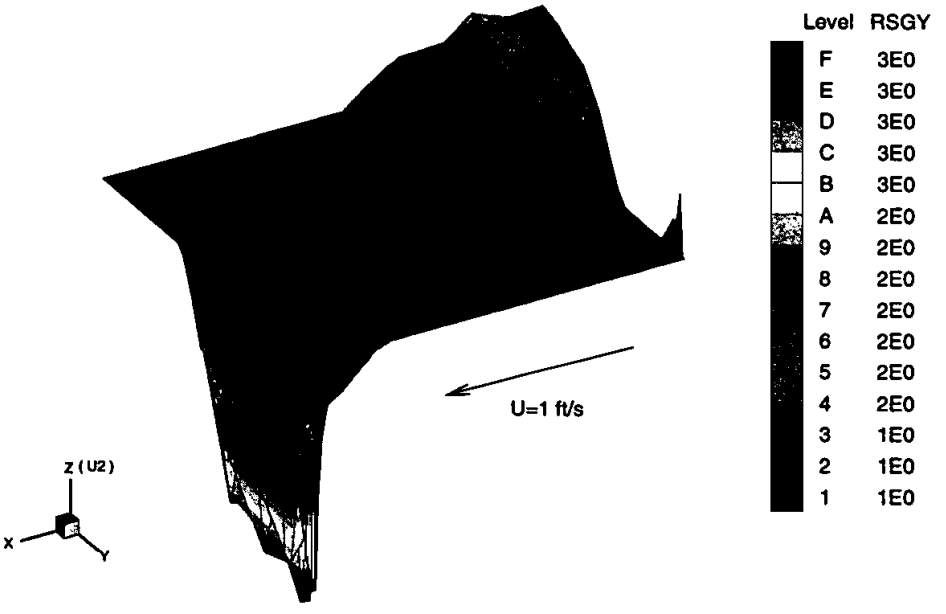

(*b*)

Figure 8. Nodal distribution of SGM^h parameter RSGM for driven cavity (Re = 3,200) on a 289-node mesh. (*a*) $RSGM_x$ perspective view, $rsgm_x \geq 1$; (*b*) $RSGM_y$ perspective view, $rsgm_y \geq 1$.

continuity constraint algorithm, (6)–(7*b*), for 2D isothermal flow. The boundary conditions are fully developed (parabolic) laminar inlet U profile with the V inlet velocity zero and no slip on the top and bottom walls. At outflow, the Dirichlet boundary conditions for pressure and ϕ in (6)–(7*b*) were fixed at zero and the velocity boundary condition was homogeneous Neumann.

Figure 9 summarizes GWS^h algorithm-computed velocity vector distributions for $100 \leqslant \mathrm{Re} \leqslant 800$, as obtained on a nominal-density $7 \times 18 + 48 \times 35$ nonuniform mesh. The arrows perpendicular to the duct walls indicate the primary and secondary recirculation reattachment coordinates reported in [27]. The solution for the primary reattachment coordinate for $100 \leqslant \mathrm{Re} \leqslant 400$, Figures 9*a*–9*c*, agrees essentially exactly with the experimental data, and the steady solution predicts the insipient secondary region at Re = 400. However, agreement with data degrades sharply with increasing Reynolds number for Re > 400, as the intrinsic GWS^h algorithm dispersive error mechanism yields an unsteady secondary separation bubble that never achieves steady state, Figures 9*d*–9*e*. Figure 10 summarizes data for a range of unsuccessful CFD attempts to obtain a 2D steady-state and accurate solution for $100 \leqslant \mathrm{Re} \leqslant 800$.

The application of SGM^h in promoting monotonicity, hence controlling the GWS^h dispersion error mechanism, constitutes the critical Re = 800 validation. The velocity vector fields computed using the GWS^h, dissipative TWS^h, and a statically condensed (but not SGM^h) quadratic-basis GWS^h algorithm (labeled p-WS^h), and the SGM^h algorithm are compared in Figures 11*a*–11*e*. The arrows labeled x_1/S, x_4/S, and x_5/S indicate the measured primary and secondary reattachment coordinates [27]. The GWS^h and p-WS^h algorithms did not produce steady-state solutions on this mesh (these data are "snapshots" in the unsteady solution). The TWS^h steady solution comparisons confirm that inaccuracy in predicting the shallow upper-surface secondary recirculation bubble leads to errors of the order 20% in primary recirculation reattachment location. Conversely, the SGM^h algorithm solution primary reattachment coordinate (x_1/S) error is about 2%, as the shallow secondary recirculation region is contained in span and with extent within 95% agreement with data, although the x_4 intercept is displaced 0.15 x_1/S units downstream of the data. The SGM^h data for primary recirculation attachment for $400 \leqslant \mathrm{Re} \leqslant 800$ are included in Figure 10, and clearly confirm superior accuracy for the range of solution data plotted.

The monotonicity issue distinctions are graphically enforced using perspective plotting of speed isosurfaces. The comparison U (scalar) perspective plots for the GWS^h, TWS^h, and p-WS^h algorithms at Re = 800, Figures 12*a*–12*d*, clearly show the $2\,\Delta x$ error mode as "color diamonds" in the (−0.15–0.016), yellow (1.0–1.2), and lemon yellow (0.84–1.0) ranges. The linear basis GWS^h solution is clearly the most dispersive, while the two TWS^h solutions show selective improvement of this error mode. The larger $\beta = 0.20$ TWS^h solution, Figure 12*c*, does dissipate essentially all local mesh-scale error. The nonartificially dissipative quadratic basis p-WS^h solution, Figure 12*d*, shows an increasing region of yellow level, while evidencing modest nonmonotonicity in the orange-red diamonds. In clear distinction, the SGM^h algorithm solution, Figure 12*e*, is genuinely monotone, showing no dispersion error (color diamonds). As a consequence, the ranges of red (1.2–1.3) and yellow (0.84–1.0) fully extend into the solution domain, yielding the indicated

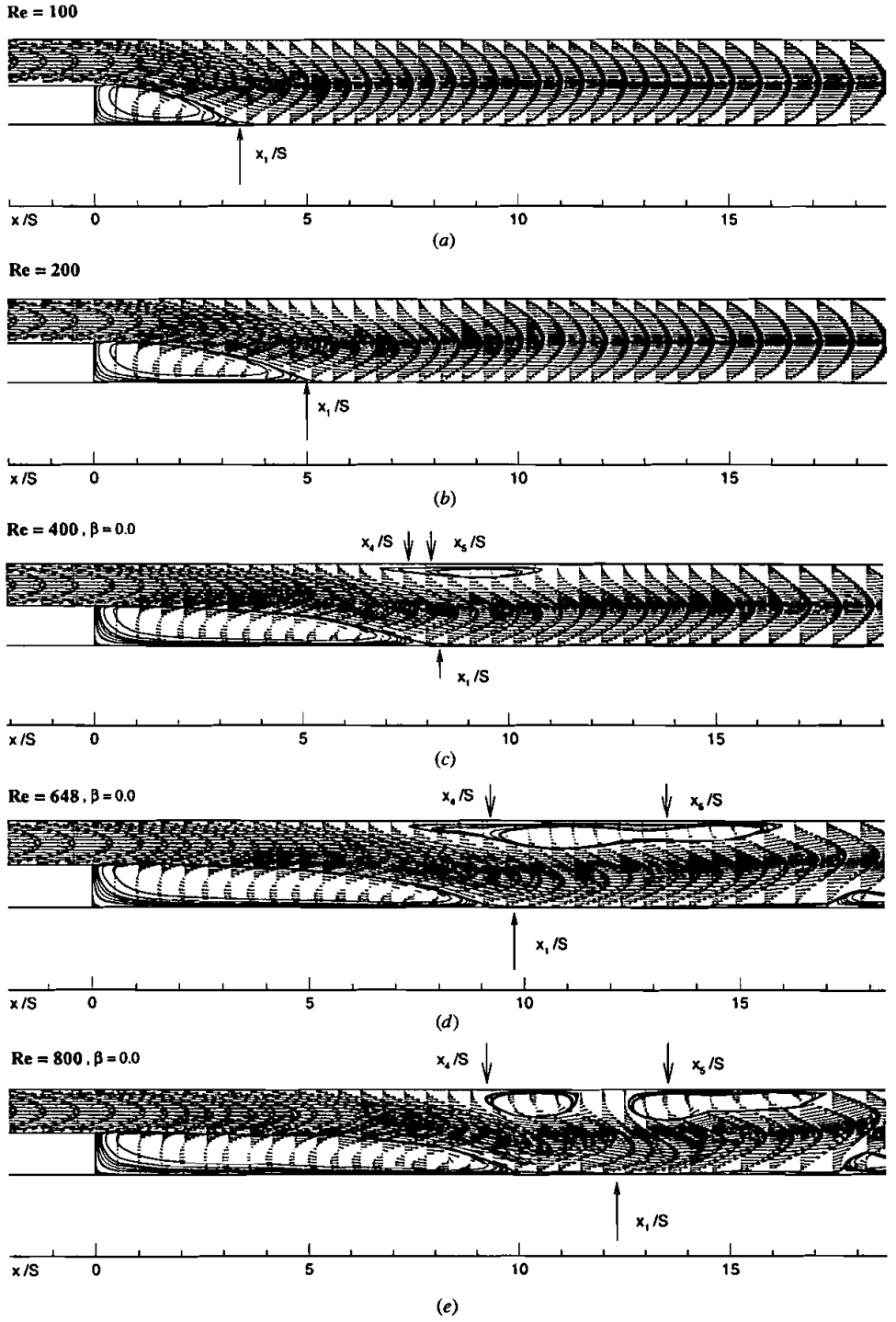

Figure 9. GWS^h solutions for 2D backward-facing step, $100 \leq \mathrm{Re} \leq 800$, on a nonuniform $7 \times 18 + 48 \times 35$ node mesh.

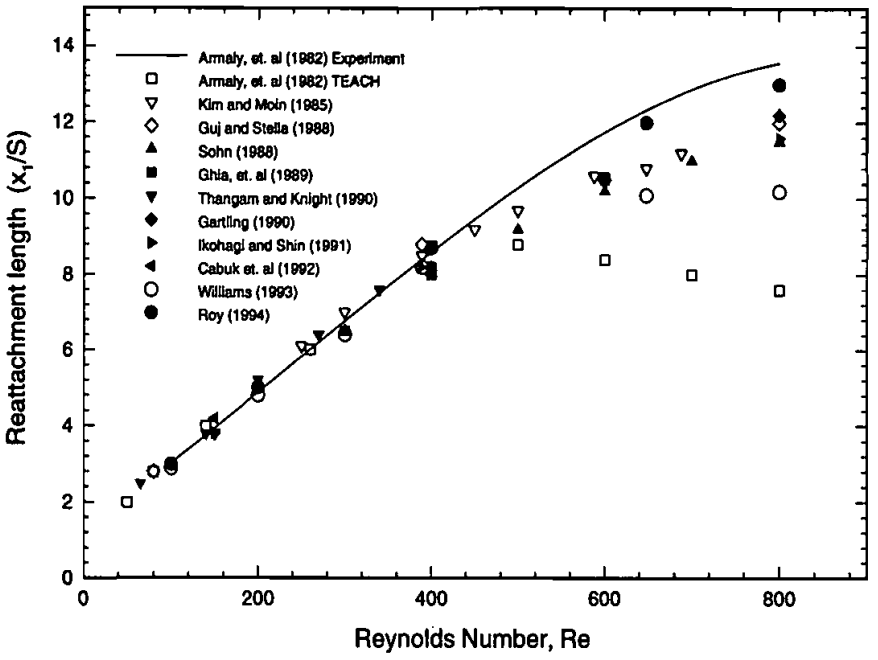

Figure 10. Primary recirculation reattachment coordinate, various solutions for $100 \leqslant \mathrm{Re} \leqslant 800$.

agreement with the primary recirculation data. The companion presentation for V solutions, with mesh overlays for emphasis, is presented in Figure 13.

Figure 14 summarizes the SGM nonlinearly determined algorithm parameter sets rsgm_x and rsgm_y, computed during the iterative solution process according to (35), as a function of nodal velocity components, and the local directional mesh measures, h_x and h_y and Re. The near-step finite-element mesh and SGM^h U and V speed solutions are also shown in perspective. The SGM^h theory parameter extrema are logically correlated with velocity and mesh coarseness, Figures $14d$–$14e$, and the rsgm_j levels for U are three orders larger than for V. The data of Figure $14d$ could logically lead to a solution-adaptive meshing strategy, to restrict the local variation in rsgm_j, hence reduce the SGM^h intrinsic dissipative levels.

CONCLUSIONS

The subgrid embedded (SGM) Lagrange finite-element basis construction has been implemented, verified, and benchmarked for semidiscrete approximate constructions of Galerkin weak statements for steady Navier-Stokes applications. Element-level static condensation of the SGM Lagrange basis $S \geqslant 2$ diffusion matrix facilitates embedding of arbitrary-degree polynomials, guaranteeing the minimal storage requirement associated with a $k = 1$ Lagrange-basis algorithm.

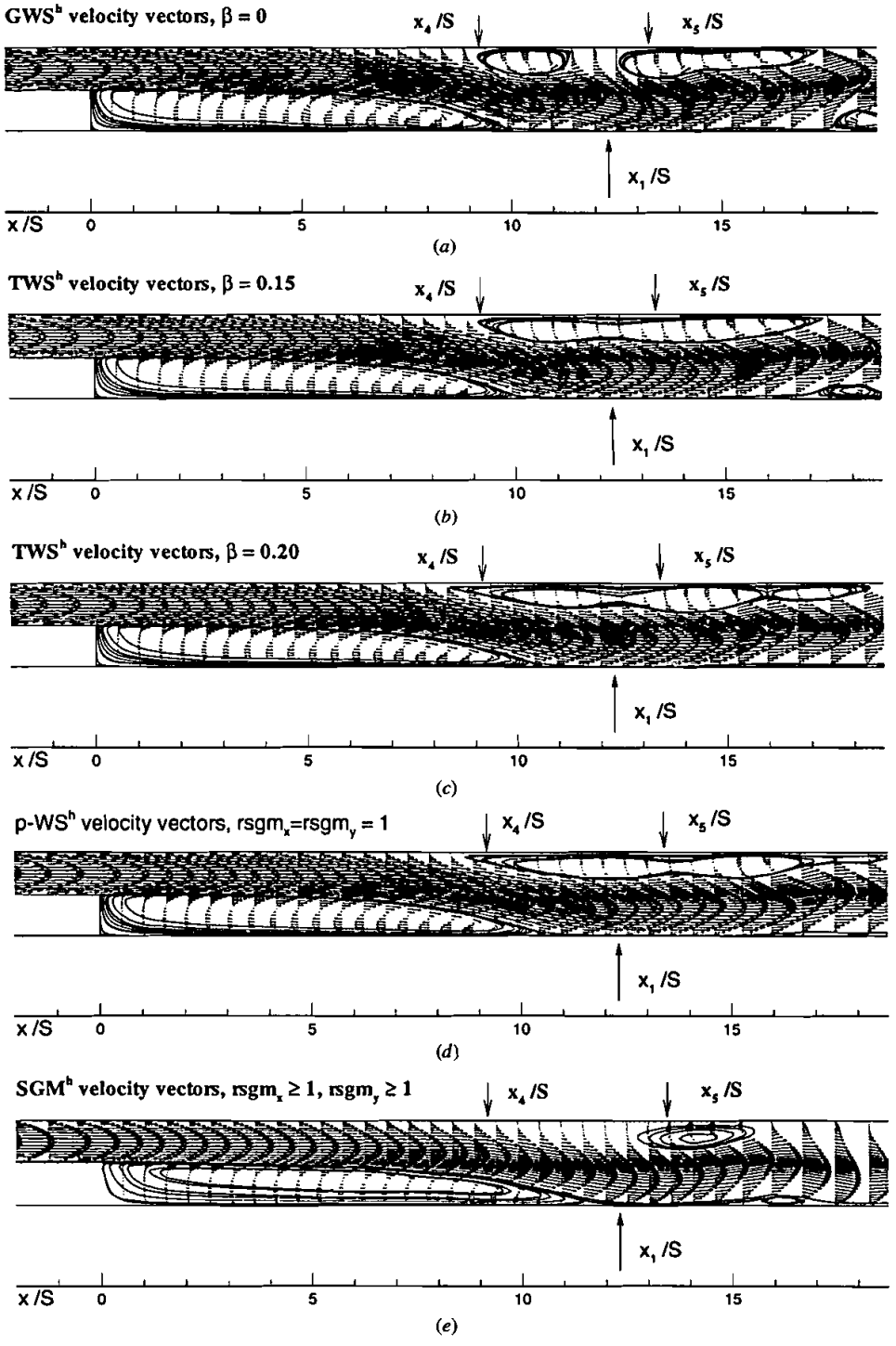

Figure 11. Comparison velocity vectors for 2D backward-facing step, Re = 800, nonuniform 7 × 18 + 48 × 35 node mesh.

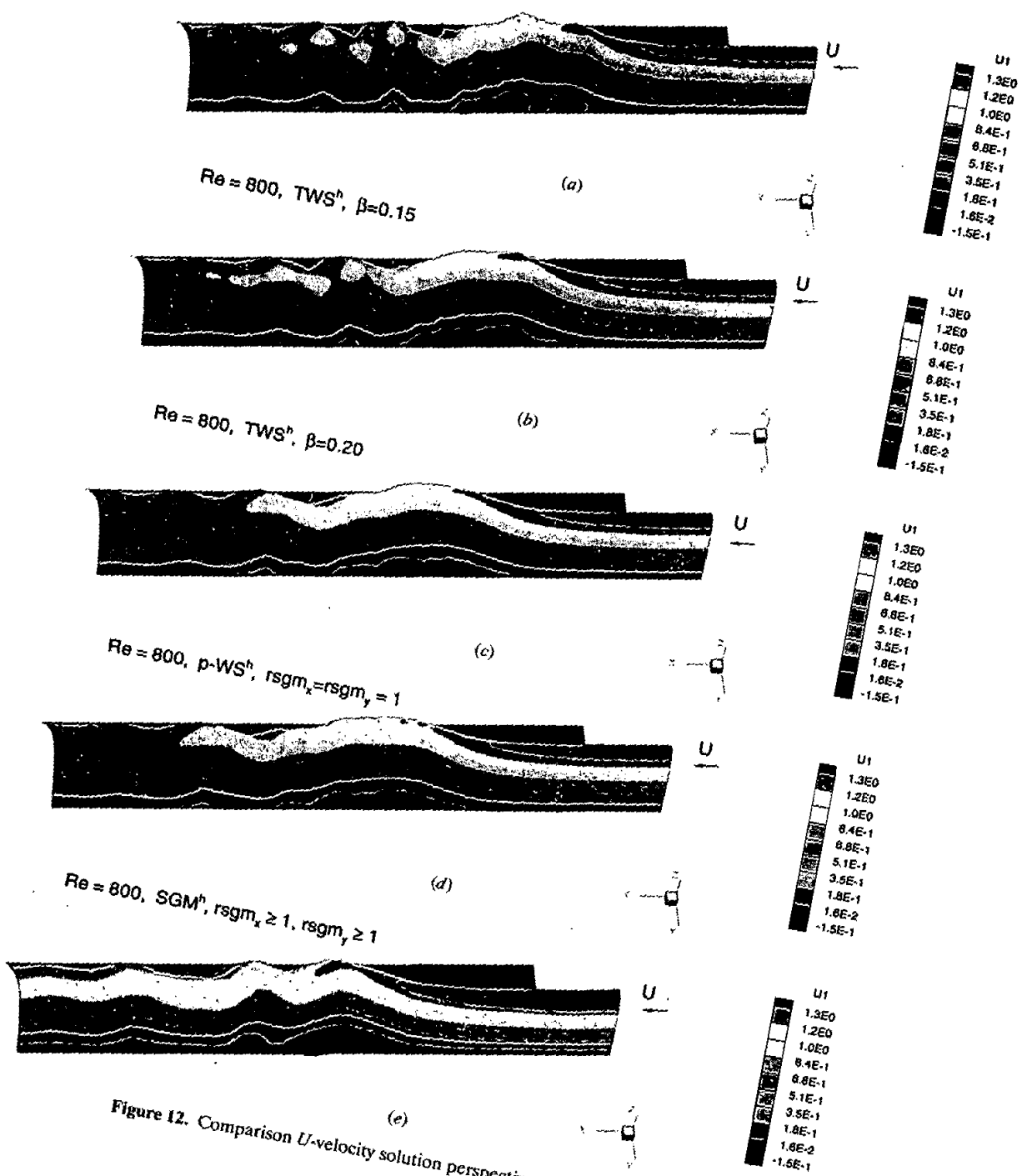

Figure 12. Comparison U-velocity solution perspective views, Re = 800.

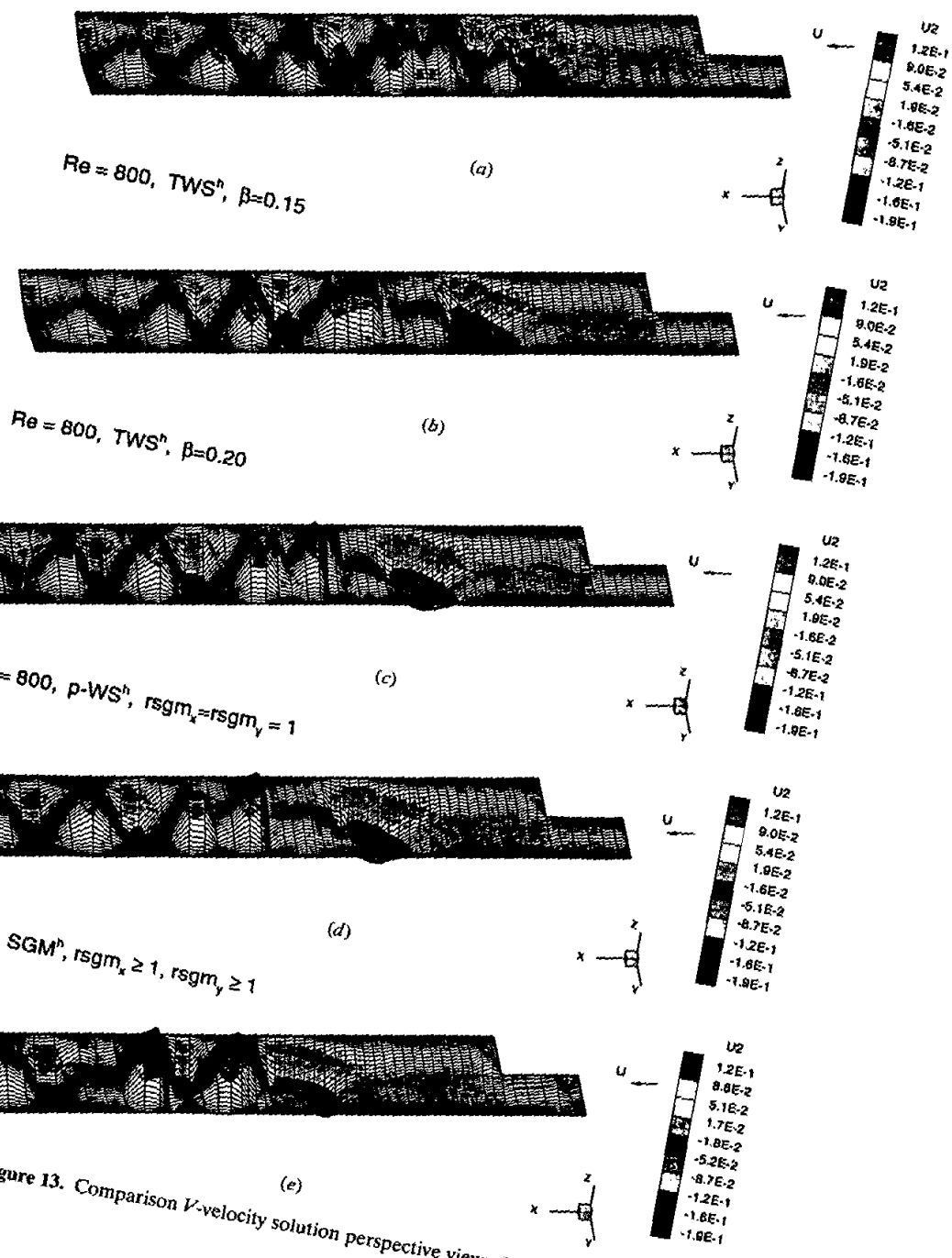

Figure 13. Comparison V-velocity solution perspective views, $Re = 800$.

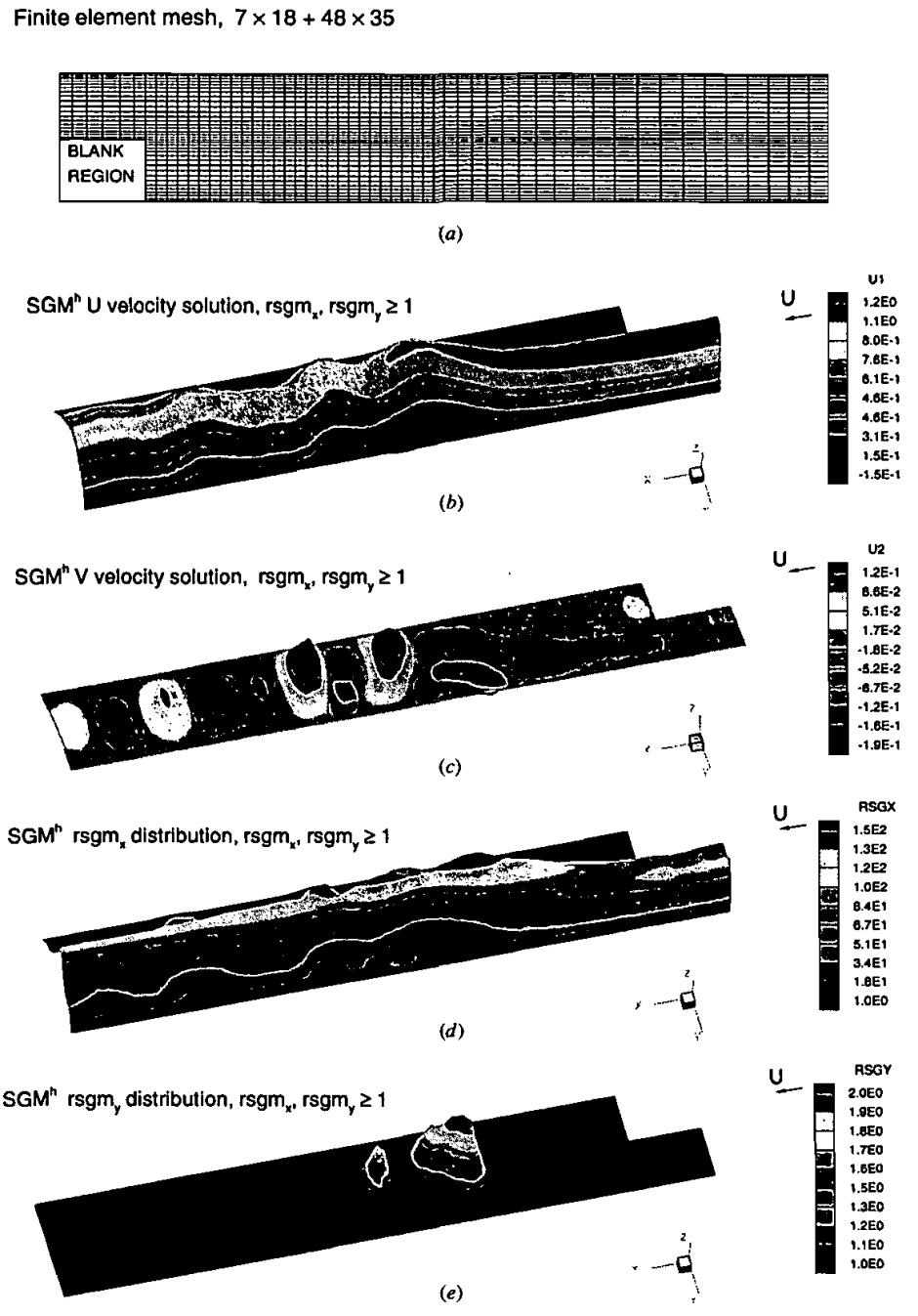

Figure 14. SGM^h solution perspective details for 2D backward-facing step, Re = 800.

The presented results confirm the theory for both compressible and incompressible Navier-Stokes applications. In comparison to other theories for generating higher-order-accurate and/or monotone solutions, the SGM element advantages include guaranteed (nonlinear) monotone solution, excellent conditioning of the *minimum-band* system matrix, and *improved stability* via retained diagonal dominance. Further, the SGM methodology permits retention of lexicographic ordering for any embedding degree, hence exhibits the efficiency of strictly linear basis (or centered FD) algorithms. The SGM finite-element Galerkin weak statement algorithm thus exhibits the potential for fundamental impact on CFD methodology, via its intrinsic nonlinearity and guarantee of minimum computer memory and CPU requirements for high-accuracy monotone solutions on relatively coarse meshes on $\Re^3$.

REFERENCES

1. A. J. Baker and J. W. Kim, A Taylor Weak Statement Algorithm for Hyperbolic Conservation Laws, *Int. J. Numer. Meth. Fluids*, vol. 7, pp. 489–520, 1987.
2. P. D. Lax, Weak Solutions of Nonlinear Hyperbolic Equations and Their Numerical Computation, *Commun. Pure Appl. Math.*, vol. 7, pp. 159–193, 1954.
3. H. O. Kreiss and J. Lorenz, *Initial-Boundary Value Problems and the Navier-Stokes Equations*, Academic Press, New York, 1989.
4. J. P. Boris and D. L. Book, Fully Multi-dimensional Flux-Corrected Transport Algorithms for Fluids, *J. Comput. Phys.*, vol. 11, pp. 38–69, 1973.
5. S. T. Salezak, Flux-Corrected Transport, I. SHASTA, a Fluid Transport Algorithm that Works, *J. Comput. Phys.*, vol. 31, pp. 355–362, 1979.
6. B. Van Leer, *Proc. 8th Int. Conf. on Numerical Methods in Fluid Dynamics*, Springer-Verlag, 1982.
7. H. T. Huynh, Accurate Monotone Cubic Interpolation, *SIAM J. Numer. Anal.*, vol. 30, pp. 57–100, 1993.
8. I. Babuška, B. Q. Guo, and E. P. Stephan, On the Exponential Convergence of the *h-p* Version for Boundary Element Galerkin Methods on Polygons, *Math. Meth. Appl. Sci.*, vol. 12, pp. 413–427, 1990.
9. L. Demkowicz, A. Karafiat, and J. T. Oden, Solution of Elastic Scattering Problems in Linear Acoustics Using *h-p* Boundary Element Method, *Comput. Meth. Appl. Mech. Eng.*, vol. 101, pp. 251–282, 1992.
10. S. Jensen, *p*-Version of Mixed Finite Element Methods for Stokes-like Problems, *Comput. Meth. Appl. Mech. Eng.*, vol. 101, pp. 27–41, 1992.
11. C. Johnson and P. Hansbo, Adaptive Finite Element Methods in Computational Mechanics, *Comput. Meth. Appl. Mech. Eng.*, vol. 101, pp. 143–181, 1992.
12. J. T. Oden, Optimal *hp*-Finite Element Methods, TICOM Rep. 92-09, Texas Institute for Computational Mechanics, University of Texas, Austin, TX, 1992.
13. O. C. Zienkiewicz, D. W. Kelly, J. Gago, and I. Babuska, Hierarchical Finite Element Approaches, Error Estimates and Adaptive Refinement, in J. Whiteman (ed.), *The Mathematics of Finite Elements and Applications IV*, pp. 311–346, Academic Press, New York, 1982.
14. O. C. Zienkiewicz and J. Z. Zhu, The Superconvergent Patch Recovery (SPR) and Adaptive Finite Element Refinement, *Comput. Meth. Appl. Mech. Eng.*, vol. 101, pp. 207–224, 1992.

15. S. Roy and A. J. Baker, Non-linear Subgrid Embedded Finite Element Basis for Accurate, Monotone, Steady CFD Solutions, *Numer. Heat Transfer. B*, vol. 31, pp. 135–176, 1997.
16. J. T. Oden, Optimal *h-p* Finite Element Methods, *Comput. Meth. Appl. Mech. Eng.*, vol. 112, pp. 309–331, 1994.
17. T. J. R. Hughes, Multiscale Phenomena: Green's Functions, the Dirichlet-to-Neumann Formulation, Subgrid Scale Models, Bubbles and the Origins of Stabilized Methods, *Comput. Meth. Appl. Mech. Eng.*, vol. 127, pp. 387–401, 1995.
18. S. Roy, On Improved Methods for Monotone CFD Solution Accuracy, Ph.D. thesis, University of Tennessee, Knoxville, TN, 1994.
19. W. Jaunzemis, *Continuum Mechanics*, Macmillan, New York, 1967.
20. P. T. Williams and A. J. Baker, Incompressible Computational Fluid Dynamics and the Continuity Constraints Method for the Three-Dimensional Navier-Stokes Equations, *Numer. Heat Transfer B*, vol. 29, pp. 137–273, 1996.
21. M. S. Liou and B. van Leer, Choice of Implicit and Explicit Operators for the Upwind Differencing Method, Tech. Paper AIAA 88-0624 26th Aerospace Meeting, Reno, NV, 1988.
22. U. Ghia, K. N. Ghia, and C. T. Shin, High-Re Solutions for Incompressible Flow Using the Navier-Stokes Equations and a Multigrid Method, *J. Comput. Phys.*, vol. 48, pp. 387–411, 1982.
23. M. Nallasamy and K. K. Prasad, On Cavity Flow at High Reynolds Number, *J. Fluid Mech.*, vol. 9, p. 391, 1977.
24. S. G. Rubin and P. K. Khosla, Polynomial Interpolation Methods for Viscous Flow Calculations, *J. Comput. Phys.*, vol. 24, pp. 217–244, 1977.
25. B. N. Jiang, A Least-Squares Finite Element Method for Incompressible Navier-Stokes Problems, NASA TM 102385, ICOMP-89-28, 1989.
26. A. J. Baker, *Finite Element Computational Fluid Mechanics*, Taylor & Francis, Washington, D.C., 1983.
27. B. F. Armaly, F. Durst, J. C. F. Pereira, and B. Schönung, Experimental and Theoretical Investigation of Backward-Facing Step Flow, *J Fluid Mech.*, vol. 127, pp. 473–496, 1983.
28. K. N. Ghia, G. A. Osswald, and U. Ghia, Analysis of Incompressible Massively Separated Viscous Flows Using Unsteady Navier-Stokes Equations, *Int. J. Numer. Meth. Fluids*, vol. 9, pp. 1025–1050, 1989.
29. D. K. Gartling, A Test Problem for Outflow Boundary Conditions—Flow over a Backward-Facing Step, *Int. J. Numer. Meth. Fluids*, vol. 11, pp. 953–967, 1990.
30. P. M. Gresho, D. K. Gartling, K. A. Cliffe, T. J. Garratt, A. Spence, K. H. Winters, J. H. Goodrich, and J. R. Torczynski, Is the Steady Viscous Incompressible 2D Flow over a Backward-Facing Step at Re = 800 Stable?, *Int. J. Numer. Meth. Fluids*, vol. 17, pp. 501–541, 1993.